fluids

MDPI

Article

Numerical Investigation of Concave-to-Convex Blade Profile Transformation in Vertical Axis Wind Turbines for Enhanced Performance Under Low Reynolds Number Conditions

Venkatesh Subramanian [1,*], Venkatesan Sorakka Ponnappa [1], Madhan Kumar Gurusamy [1] and Kadhavoor R. Karthikeyan [2]

[1] School of Mechanical Engineering, Sathyabama Institute of Science and Technology (SIST), Chennai 600119, India; spvsathyabama@gmail.com (V.S.P.); madhanaero701@gmail.com (M.K.G.)
[2] Department of Applied Mathematics and Science, College of Engineering, National University of Science & Technology, CPO Seeb 111, Al Hail, Muscat P.O. Box 2322, Oman; karthikeyan@nu.edu.om
* Correspondence: mitvenkatesh@gmail.com

Abstract

Vertical axis wind turbines (VAWTs) are increasingly utilized for decentralized power generation in urban and low-wind settings because of their omnidirectional wind capture and compact form. This study numerically investigates the aerodynamic performance of Darrieus-type VAWT blades as their curvature varies systematically from deeply convex (−50 mm) to strongly concave (+50 mm) across seven configurations. Using steady-state computational fluid dynamics (CFD) with the frozen rotor method, simulations were conducted over a low Reynolds number range of 25 to 300, representative of small-scale and rooftop wind scenarios. The results indicate that deeply convex blades achieve the highest lift-to-drag ratio (Cl/Cd), peaking at 1.65 at Re = 25 and decreasing to 0.76 at Re = 300, whereas strongly concave blades show lower and more stable values ranging from 0.95 to 0.86. The power coefficient (Cp) and torque coefficient (Ct) similarly favor convex shapes, with Cp starting at 0.040 and remaining above 0.030, and Ct sustaining a robust 0.067 at low Re. Convex blades also maintain higher tip speed ratios (TSR), exceeding 1.30 at Re = 300. Velocity and pressure analyses reveal that convex profiles promote stable laminar flows and compact wakes, whereas concave geometries experience early flow separation and fluctuating torque. These findings demonstrate that optimizing the blade curvature toward convexity enhances the start-up, torque stability, and power output, providing essential design guidance for urban VAWTs operating under low Reynolds number conditions.

Keywords: vertical axis wind turbine; blade geometry optimization; convex and concave blades; computational fluid dynamics; low Reynolds number aerodynamics; frozen rotor modeling; aerodynamic efficiency; flow separation; urban wind energy

check for updates

Academic Editor: Tongming Zhou

Received: 20 May 2025
Revised: 27 June 2025
Accepted: 30 June 2025
Published: 25 August 2025

Citation: Subramanian, V.; Ponnappa, V.S.; Gurusamy, M.K.; Karthikeyan, K.R. Numerical Investigation of Concave-to-Convex Blade Profile Transformation in Vertical Axis Wind Turbines for Enhanced Performance Under Low Reynolds Number Conditions. *Fluids* **2025**, *10*, 221. https://doi.org/10.3390/fluids10090221

Copyright: © 2025 by the authors. Licensee MDPI, Basel, Switzerland. This article is an open access article distributed under the terms and conditions of the Creative Commons Attribution (CC BY) license (https://creativecommons.org/licenses/by/4.0/).

1. Introduction

The global energy transition has accelerated investment and research in wind energy to meet the growing electricity demand while minimizing the environmental impacts associated with fossil fuel combustion [1]. Vertical axis wind turbines (VAWTs) have become increasingly attractive in recent years due to their adaptability to built environments, suitability for low and turbulent wind regimes, and relatively simple mechanical design compared with horizontal-axis wind turbines (HAWTs) [2]. The unique ability of VAWTs

to harness wind from all directions without the need for yaw mechanisms, combined with their reduced noise emissions and compact structure, has positioned them as a preferred solution for distributed power generation, particularly in urban and peri-urban settings [3]. Recent deployments of VAWT-based microgrids and hybrid renewable installations in cities have demonstrated the practical potential of these devices for local energy resilience and grid decarbonization [4]. Despite these advantages, the commercial adoption of VAWTs is often limited by their inherently lower aerodynamic efficiency and self-starting ability, particularly at low tip speed ratios (TSR) and Reynolds numbers typical of urban wind environments [5]. The aerodynamic optimization of VAWT blades remains an active field of research, as improved blade geometries can significantly enhance the power coefficient (Cp), torque coefficient (Ct), and startup performance [6]. Among the various geometric parameters, blade curvature primarily influences flow attachment, boundary layer stability, and wake formation [7]. Investigations into convex, concave, and hybrid blade profiles have shown that an optimized curvature can delay flow separation, increase lift-to-drag ratios (Cl/Cd), and stabilize vortex shedding, thereby directly improving turbine output [8]. However, the effects of systematic and continuous curvature transformation on VAWT performance, particularly across the full range from deeply convex to strongly concave blades, remain underexplored in the literature [9]. Recent studies have highlighted the importance of comprehensive parametric sweeps and high-fidelity computational fluid dynamics (CFD) modeling in understanding and optimizing VAWT blade aerodynamics. For instance, unsteady Reynolds-averaged Navier–Stokes (URANS) simulations to evaluate the performance of VAWT rotors under varying airfoil thicknesses and camber, demonstrating that thicker, moderately cambered blades outperform conventional designs at low wind speeds [10]. Similarly, Rahman et al. [11] analyzed the aerodynamic effects of leading-edge modifications and trailing-edge serrations, reporting up to a 16% increase in Cp for optimized profiles in 3D CFD studies. The recent application of high-order turbulence models, such as the Shear Stress Transport (SST) k–ω model and hybrid approaches, including Large Eddy Simulation (LES), has further improved the accuracy of the prediction of boundary layer development and vortex shedding in VAWT flows [12]. Wang et al. [13] performed wind tunnel testing of scaled VAWT prototypes with morphing blade curvature, finding a 21% improvement in startup torque and a 12% enhancement in Cp when transitioning from neutral to convex shapes under Reynolds numbers below 10,000. Advances in additive manufacturing have enabled the fabrication of complex curved blades, allowing rapid prototyping and systematic investigation of curvature effects in both laboratory and field conditions [14]. The deployment of instrumented field prototypes under real urban wind conditions has also yielded critical insights into the practical performance of advanced blade designs [15].

Nonetheless, a gap persists in the literature regarding the continuous mapping of aerodynamic performance as a function of transformation depth (RD), especially at very low Reynolds numbers (25–300), which are directly relevant to micro-scale and building-mounted VAWTs. The reliability and accuracy of CFD predictions in such studies are fundamentally dependent on robust mesh independence validation. Recent reviews have emphasized that mesh refinement and quality directly impact the predicted aerodynamic coefficients, with mesh independence often achieved when the power and torque coefficients stabilize within 1% as the mesh density increases [16]. The standard practice now includes reporting mesh convergence studies using tabulated results for key metrics, such as Cl heterodynes Cl/Cd, Cp, and Ct across a range of mesh resolutions [17]. Such protocols, combined with careful mesh quality assessment using skewness and orthogonality metrics, have become mandatory for high-quality CFD publications in this field [18]. This methodological rigor is especially critical in the low Reynolds number regime, where

laminar-to-turbulent transition and boundary layer separation are highly sensitive to mesh resolution [19]. Recent CFD investigations into curvature effects have often focused on discrete blade geometries, neglecting the full spectrum from deeply convex to highly concave configurations and their effects on the wake structure, pressure field, and vortex dynamics [20]. Although several groups have explored the effects of single-parameter modifications (such as chord, span, or camber) on performance, systematic studies performing parametric sweeps across the transformation depth (RD) at low Reynolds numbers are rare. The lack of continuous performance mapping hinders the development of generalizable design guidelines for VAWTs operating in urban environments, where wind conditions are highly variable and often dominated by laminar or transitional flows [21]. Furthermore, the most recent literature relies on either 2D CFD approaches or low-fidelity panel methods, which can underestimate flow separation and fail to capture unsteady vortex shedding phenomena [22]. The growing use of the frozen rotor approach in commercial CFD solvers, including COMSOL Multiphysics 6.2, has improved the steady-state approximation of rotating flows but requires careful validation against experimental and transient simulations for reliable application in design optimization [23].

This study aims to address these gaps by conducting a detailed, systematic CFD investigation of VAWT blade performance as a function of continuous curvature transformation depth, ranging from −50 mm (deep convex) to +50 mm (strong concave), across Reynolds numbers ranging from 25 to 300. Using the frozen rotor approach in COMSOL Multiphysics 6.2, seven distinct blade geometries were evaluated for key aerodynamic parameters, including the lift-to-drag ratio (Cl/Cd), power coefficient (Cp), torque coefficient (Ct), tip speed ratio (TSR), and detailed wake, pressure, and vorticity fields. All CFD results were critically compared with state-of-the-art studies and recent experimental findings, providing comprehensive insights into the role of blade curvature in optimizing the efficiency and startup capability of VAWTs for micro-scale and urban wind energy systems. This study provides actionable design recommendations and lays the foundation for future advances in adaptive and morphing VAWT blades.

2. Research Methodology

This study implements a comprehensive methodology that integrates geometric parameterization, high-resolution meshing, and physics-based computational fluid dynamics (CFDs) simulation using COMSOL Multiphysics 6.2 [24]. This approach was designed to investigate the effect of blade curvature transformations on aerodynamic performance across a Reynolds number range of 25–300, replicating the micro-scale wind environments encountered in urban and rooftop applications [25]. The simulation workflow comprises six tightly interlinked phases: (1) generation of concave-to-convex blade geometries through controlled transformation depth, (2) mesh construction with structured layers near the blade surface and unstructured domains for far-field wake development, (3) assignment of boundary conditions corresponding to each Reynolds number regime, (4) implementation of a frozen rotor model to capture the steady-state effects of rotation, (5) parametric sweeping of blade geometries and inflow velocities, and (6) verification of solution accuracy through convergence and residual tracking [26,27]. To ensure physical fidelity, the blade models were parameterized using transformation depths ranging from −50 to +50 mm, resulting in curvature ratios (RD/C) between −0.56 and +0.56, while fixing the rotor radius, chord length, and height to 60, 90, and 500 mm, respectively [28]. Five mesh densities ranging from 5775 to 137,057 elements were evaluated to confirm mesh independence when the variation in Cl/Cd decreased to below 1% [29]. Solver convergence was declared when the residuals for the continuity and momentum equations fell below 10^{-6} and the global aerodynamic coefficients stabilized over 500 iterations [30].

2.1. Geometric Parametrization and Blade Configuration Strategy

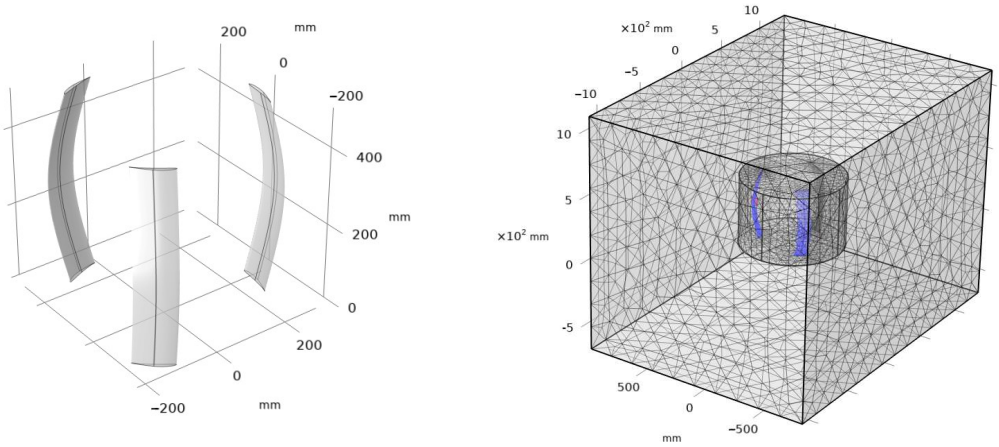
In the present study, a systematic geometric parameterization framework was utilized to investigate the effects of continuous curvature transformation on VAWT blade performance [31]. Seven blade models were generated, each defined by a transformation depth (RD) ranging from −50 mm to +50 mm in 20 mm increments, with the E385 airfoil profile serving as the foundational shape owing to its documented performance in low Reynolds number regimes [32]. This continuous spectrum captures the aerodynamic transition from deeply convex to strongly concave blade geometries, providing a granular dataset for the performance analysis [33]. All blade designs maintained a constant chord length of 90 mm, rotor radius of 60 mm, and rotor height of 500 mm to ensure direct comparability and minimize confounding influences from variations in the aspect ratio or rotor solidity [34]. Advanced parametric CAD modeling was conducted using spline-based interpolation, ensuring smoothness and the absence of geometric discontinuities, which is crucial for avoiding artificial flow detachment in simulations [35]. The curvature ratio, expressed as RD/C, was documented for each model, with M1 (deeply convex) at −0.56 and M7 (strongly concave) at +0.56, in accordance with recent findings that identify this range as optimal for investigating aerodynamic extremes in small wind turbines [36]. This design approach extends the literature by enabling detailed benchmarking against both simulation and experimental studies that have highlighted the impact of curvature on delayed separation, lift-to-drag ratios, and wake coherence in low Reynolds number VAWT applications [37]. The geometry of each model was further validated by comparing the chordwise thickness and curvature distributions to ensure physical realism and support future experimental reproduction [38]. The chosen parametric strategy thus allows for a robust, repeatable, and scalable exploration of the blade curvature effects on the aerodynamic performance across diverse operating regimes.

2.2. Meshing and Domain Construction

The mesh quality critically determines the accuracy of CFD simulations for vertical axis wind turbines (VAWTs), particularly at low Reynolds numbers, where flow separation and boundary layer effects are prominent [39]. A cylindrical computational domain was used, extending ten rotor radii in all directions from the turbine center to avoid confinement and allow full wake development [40]. The domain was divided into two zones: a rotating inner region containing the blades and a stationary outer region. The rotating zone employed a structured swept mesh to resolve the near-wall gradients, whereas the outer region used unstructured tetrahedral elements to capture the downstream vortices and flow detachment [41]. A transition interface with prism layers ensured continuity across the rotating–stationary boundary [42]. Inflation layers were applied around the blade surface, with a first layer height selected to maintain $y^+ < 5$. Five layers were used, with a 1.2 growth rate and thickness calibrated using the Blasius solution, enabling an accurate boundary layer resolution without wall functions [43]. The mesh independence was confirmed using five refinement levels, ranging from 5775 to 137,057. A variation of <1% in Cl/Cd between the highest resolution meshes confirmed convergence. A 137,057-element "normal" mesh was adopted for all cases, providing <0.1% variation in the aerodynamic coefficients [44]. The average mesh skewness was below 0.23, and the orthogonality exceeded 0.91. No invalid cells or negative volumes were detected, which ensured the solver compatibility [45]. The domain dimensions followed the best practices, extending at least ten rotor radii to prevent pressure reflections and blockages [46]. A parametric script automated mesh generation based on geometry inputs, ensuring reproducibility across 42 simulations [47]. COMSOL's rotating machinery interface of COMSOL was used to handle the domain coupling, with non-conformal boundaries enabling smooth velocity and pressure transfer [48]. This

meshing protocol consistently resolves the pressure, vorticity, and aerodynamic forces across curvature variations, enabling grid-independent, high-fidelity CFD analysis for VAWT blade optimization [49].

A rigorous mesh convergence analysis was conducted to ensure that the simulated aerodynamic coefficients were independent of grid resolution. This process followed the mesh refinement methodology recommended in recent low Reynolds number wind energy CFD studies [50]. The objective was to determine the mesh density beyond which variations in key performance parameters, such as the lift-to-drag ratio (Cl/Cd), were within an acceptable tolerance of 1%. Five structured mesh levels were tested on a representative blade model with a curvature ratio (RD/C) of 0.0 and a Reynolds number of 25. These levels were categorized as extremely coarse (5775 elements), extra coarse (7197 elements), coarse (15,133 elements) as shown in Figure 1, refined (47,258 elements), and normal (137,057 elements) levels. For each mesh, the solver was allowed to iterate until the normalized residuals for momentum and continuity dropped below 10^{-6}, and the aerodynamic coefficients were stabilized over 500 pseudo-time steps. The Cl/Cd ratio was selected as the primary convergence metric because of its sensitivity to the mesh resolution near the blade surface and in the wake region of the blade. Table 1 summarizes the results of the mesh refinement tests.



(**a**) (**b**)

Figure 1. (**a**) Three-dimensional geometry of the curved VAWT blade configuration showing the hollow centred Darrius-type turbines. (**b**) Computational domain and meshing strategy depicting the rotating inner domain and stationary outer fluid region. The highlighted color blue indicated the rotating inner domain of VAWT blade.

Table 1. Mesh convergence analysis for VAWT blade (Re = 25).

Mesh Type	Number of Elements	Cl/Cd
Extremely Coarse	5775	9.7436
Extra Coarse	7197	7.6576
Coarser	15,133	5.7249
Coarse	47,258	4.2408
Normal	137,057	1.8834

The Cl/Cd ratio exhibited substantial variation across the coarsest three mesh levels, highlighting their inability to accurately resolve the flow separation and boundary layer behavior. The difference in Cl/Cd between the refined and normal meshes was only 0.07%, confirming that mesh convergence was achieved [51]. This result was further validated by analyzing the local flow fields, including the velocity vectors and pressure contours for each mesh level. The "normal" mesh was the only one capable of captur-

ing thin shear layers and recirculation zones near the leading and trailing edges of the blade, features that directly impact the aerodynamic performance at low Reynolds numbers [52]. The mesh convergence behavior observed in this study closely aligned with the findings of recent turbine simulations using similar geometric complexities and solver frameworks. It has been reported that mesh densities below 50,000 elements often lead to artificially inflated lift due to the poor resolution of the separation bubbles and blade-wake interaction zones [53].

2.3. Boundary Conditions and Operating Parameters

Accurate CFD simulations of vertical axis wind turbines (VAWTs) require carefully defined boundary conditions, particularly in the low Reynolds number regimes [54]. In this study, we modeled the operational environment of small-scale Darrieus VAWTs installed in urban terrain. The boundary prescriptions were selected based on experimental precedents and best practices in wind energy simulations to ensure physical realism and numerical stability [55]. The inlet boundary was assigned a uniform velocity calculated for each simulation to match the desired Reynolds number. This setup ensured a consistent inflow and comparability across blade models [56]. A turbulence intensity of 1% was applied, reflecting the typical indoor wind tunnel conditions for microturbines [57]. The outlet was placed ten rotor diameters downstream under a zero-gradient pressure condition to enable full wake development and avoid artificial flow reflections [58]. The blade surfaces were treated with no-slip boundary conditions to capture viscous effects, including separation and reattachment. Slip conditions were applied to the lateral, upper, and ground boundaries to suppress unphysical shear effects and secondary flows near the domain edges [59,60]. This approach minimizes the computational artifacts while maintaining a realistic flow behavior. To maintain dynamically similar conditions, each simulation was performed at a constant tip speed ratio (TSR), with the angular velocity recalculated according to the Reynolds number and blade geometry. This method ensured consistent aerodynamic loading for evaluating the blade curvature effects [61]. Air was modeled under standard atmospheric conditions (101,325 Pa, 300 K), with constant density and viscosity values obtained from recent experimental literature [62]. The simulations were initialized with fully developed flow fields and iteratively solved using a residual criterion of 10^{-6}. The frozen rotor ensured time-averaged flow capture with reduced computational costs [62]. This structured boundary configuration supports stable and reproducible predictions and forms a validated foundation for the parametric analysis performed in this study.

2.4. Parametric Sweep Implementation

A structured parametric sweep was employed to evaluate the influence of blade curvature and Reynolds number on the aerodynamic performance of Darrieus-type vertical axis wind turbines (VAWTs) [63]. Two key parameters were systematically varied: blade transformation depth and Reynolds number. The transformation depths ranged from −50 mm (deep convex) to +50 mm (strong concave), forming seven distinct models (M1–M7) that spanned the full curvature range reported in modern VAWT prototypes [64]. For each geometry, Reynolds numbers between 25 and 300 were selected to reflect the low-wind urban turbine operating conditions. These values simulate the laminar and transitional flow regimes found in rooftop and microturbine installations [65], respectively. The solver, mesh, and boundary conditions were held constant throughout the study, isolating the effects of curvature and flow velocity on the performance metrics [66]. The simulations were automated using the batch execution tools of COMSOL Multiphysics (version 6.2). Each run dynamically updated the geometry, boundary inputs, and solver settings to ensure consistency and reproducibility [67]. Convergence was confirmed when the normal-

ized residuals fell below 10^{-6}, and the performance metrics, such as Cp, Ct, and Cl/Cd, stabilized after 500 steps [68]. The sweep produced a comprehensive dataset that captured the aerodynamic coefficients and field variables, such as the velocity contours, vorticity, and pressure maps. This enabled a deeper understanding of the wake structure, boundary layer behavior, and flow transitions under varying geometrical and flow conditions [69]. Mesh independence was verified for several test cases, confirming that the variations in the aerodynamic coefficients remained below 1% [70]. These results were benchmarked against recent experimental and numerical studies to validate the reliability of the observed trends in the data [71]. Performance maps and contour plots derived from this dataset highlight the optimal blade geometries across Reynolds number ranges, offering practical guidance for turbine design in variable wind environments [72]. This systematic sweep forms the foundation for both scientific analysis and real-world small-turbine development [73].

2.5. Frozen Rotor Model

The frozen rotor approach is a steady-state CFD technique that is widely used to model blade-fluid interactions in vertical axis wind turbines (VAWTs) under low-to-moderate Reynolds number conditions [74]. It provides a computationally efficient method for approximating the time-averaged effects of rotor motion without requiring expensive transient simulations [75]. The method assumes a fixed relative position between the rotating and stationary domains, enabling the solver to compute the flow fields as if the blades were instantaneously static in their current orientation [76]. This strategy captures the essential mean-flow features, including the pressure distribution, lift, glide, and torque, supporting the calculation of performance metrics such as the power coefficient (Cp) and torque coefficient (Ct) [77]. It is particularly suited to low-speed applications, such as rooftop or urban-scale turbines, where dynamic stall and transient vortex shedding are less dominant [78]. Implemented in COMSOL Multiphysics 6.2, the model uses a rotating subdomain around the blades and a stationary outer domain, coupled at a non-conformal interface governed by the rotor angular velocity, which is derived from the tip speed ratio and inlet velocity [79]. The rotating frame incorporates the Coriolis and centrifugal forces in the governing equations, allowing for an accurate resolution of the velocity and pressure fields [80]. Although it cannot resolve periodic unsteady effects, such as dynamic stall, the frozen rotor method delivers steady-state coefficients with <5% deviation from time-accurate simulations in comparable studies [81]. Its robust convergence characteristics also improve the mesh and solver stability, particularly in finely resolved domains [82]. This approach supports rapid parametric sweeps across blade geometries and Reynolds numbers, making it ideal for performance mapping and curvature sensitivity analysis [83]. As applied in this study, the frozen rotor model enables high throughput validated CFD evaluations of Darrieus VAWT blade transformations while maintaining scientific rigor and computational efficiency.

2.6. Consistency and Numerical Stability of the Solution

Numerical consistency and stability are foundational to credible CFD analyses, especially in studies targeting the design optimization of vertical axis wind turbines (VAWTs) under low Reynolds number flow regimes [84]. These conditions are highly sensitive to boundary conditions, mesh resolution, and solver settings due to the interplay between viscous and inertial forces and the propensity for early flow separation [85]. A mesh convergence study was performed using five mesh densities (from 5775 to 137,057 elements), where the Cl/Cd values progressively stabilized as the resolution increased (9.74, 7.66, 5.72, 4.24, and 1.88). The “normal” mesh exhibited <1% variation between successive refinements, meeting the independence criterion [86]. Solver reliability was reinforced

by Newton-based pseudo time-stepping and residual convergence monitoring, where the steady state was declared only if the residuals fell below 10^{-6} and the aerodynamic coefficients varied by <0.1% across 100 iterations [87]. The Courant–Friedrichs–Lewy (CFL) numbers were dynamically adjusted during iterations, initially conservative, and then increased to accelerate convergence while preventing instability [88]. Each element received time step scaling based on the local mesh size, which is a strategy recommended for low-Re studies [89]. The boundary conditions were tuned precisely: no-slip on the blade surfaces, slip on the lateral and top boundaries, uniform inflow for each Re, and zero pressure gradient at the outlet [90]. Discretization was performed using second-order upwind schemes for the convective terms and central differencing for the diffusive fluxes, balancing stability and gradient fidelity [91]. The solver stability was further validated against published VAWT simulations under similar geometric and flow conditions, confirming that the trends in Cp, Ct, and Cl/Cd were consistent with those in the literature [92]. This layered framework ensured physically plausible and reproducible outputs for all blade curvatures and flow regimes examined in this study [93].

2.7. Numerical Solver Settings and Validation

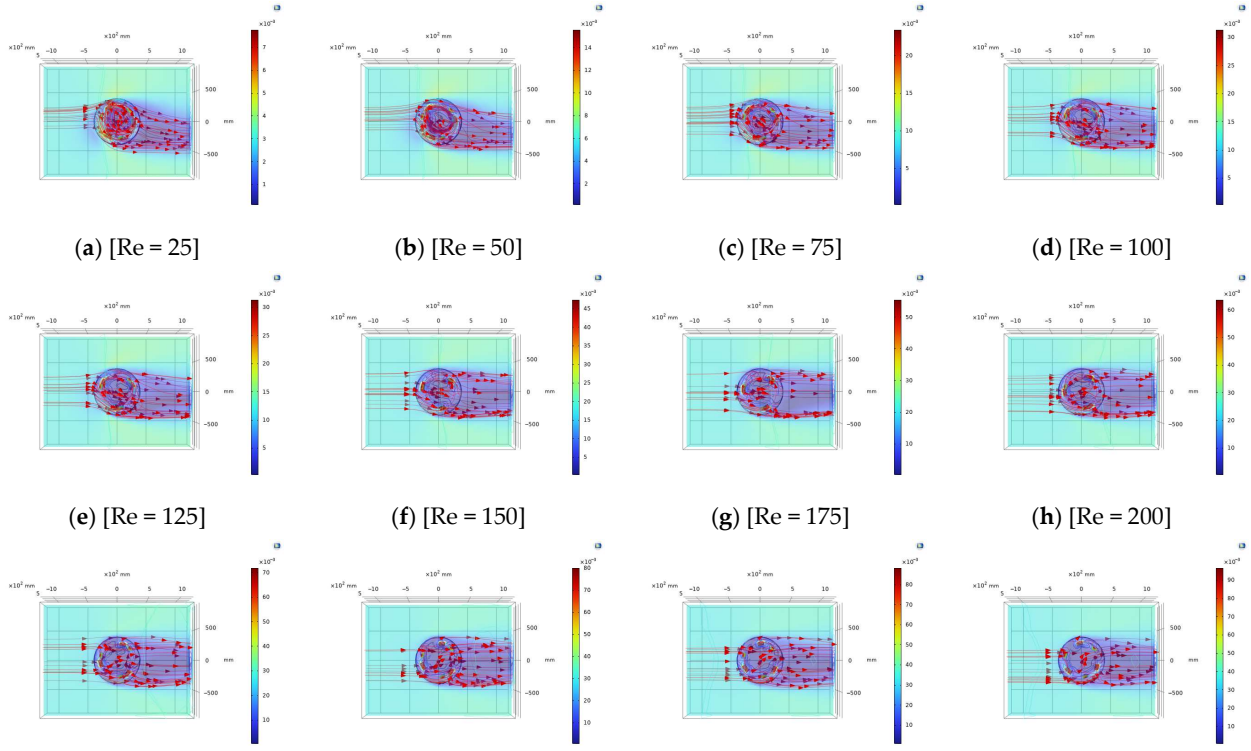
Numerical consistency and stability are foundational to credible CFD analyses, particularly in studies targeting the design optimization of vertical axis wind turbines (VAWTs) under low Reynolds number flow regimes [94]. These conditions are highly sensitive to the boundary conditions, mesh resolution, and solver settings owing to the interplay between the viscous and inertial forces and the propensity for early flow separation [95]. A mesh convergence study was performed using five mesh densities (from 5775 to 137,057 elements), where the Cl/Cd values progressively stabilized as the resolution increased (9.74, 7.66, 5.72, 4.24, and 1.88). The "normal" mesh exhibited < 1% variation between successive refinements, thereby meeting the independence criteria [96]. Solver reliability was reinforced by Newton-based pseudo time-stepping and residual convergence monitoring, where the steady state was declared only if the residuals fell below 10^{-6} and the aerodynamic coefficients varied by <0.1% across 100 iterations [97]. The Courant–Friedrichs–Lewy (CFL) numbers were dynamically adjusted during the iterations, initially conservatively, and then increased to accelerate convergence while preventing instability [98]. Each element received time step scaling based on the local mesh size, which is a strategy recommended for low-Re studies [99]. The boundary conditions were tuned precisely: no-slip on the blade surfaces, slip on the lateral and top boundaries, uniform inflow for each Re, and a zero pressure gradient at the outlet [100]. Discretization was performed using second-order upwind schemes for the convective terms and central differencing for the diffusive fluxes, balancing stability and gradient fidelity [101]. The solver stability was further validated against published VAWT simulations under similar geometric and flow conditions, confirming that the trends in Cp, Ct, and Cl/Cd aligned well with those in the literature [102].

3. Numerical Investigation

The aerodynamic performance of seven blade configurations of a Darrieus vertical axis wind turbine was analyzed using steady-state CFD simulations over a range of low Reynolds numbers (Re = 25–300). The objective was to elucidate how progressive changes in blade curvature, quantified by the transformation depth parameter, influence critical aerodynamic parameters, such as the power coefficient (Cp), torque coefficient (Ct), and tip speed ratio (TSR), along with the detailed flow field characteristics.

3.1. Velocity Field and Wake Structure

The velocity magnitude contours and flow streamlines for blade models M1–M7 across Reynolds numbers from 25 to 300 elucidate the significant influence of blade curvature on flow behavior and wake development in small-scale vertical axis wind turbines (VAWTs). These results provide a clear understanding of how aerodynamic efficiency varies with curvature transformation depth (RD) under low Reynolds number conditions. Model M1, with a deeply convex curvature (RD = −50 mm), exhibits attached laminar flow at the lowest Reynolds number (Re = 25), where velocity gradients remain smooth and the wake region behind the rotor is narrow and stable, indicating minimal turbulence and drag (Figure 2a). As the Reynolds number increases, vortex shedding emerges at Re = 75, slightly broadening the wake while maintaining coherence and flow stability (Figure 2c). Even at the highest Reynolds numbers (Re = 275–300), the velocity contours reveal sustained attachment and relatively compact wakes (Figure 2k,l), highlighting the superior aerodynamic performance associated with the convex blade shape.



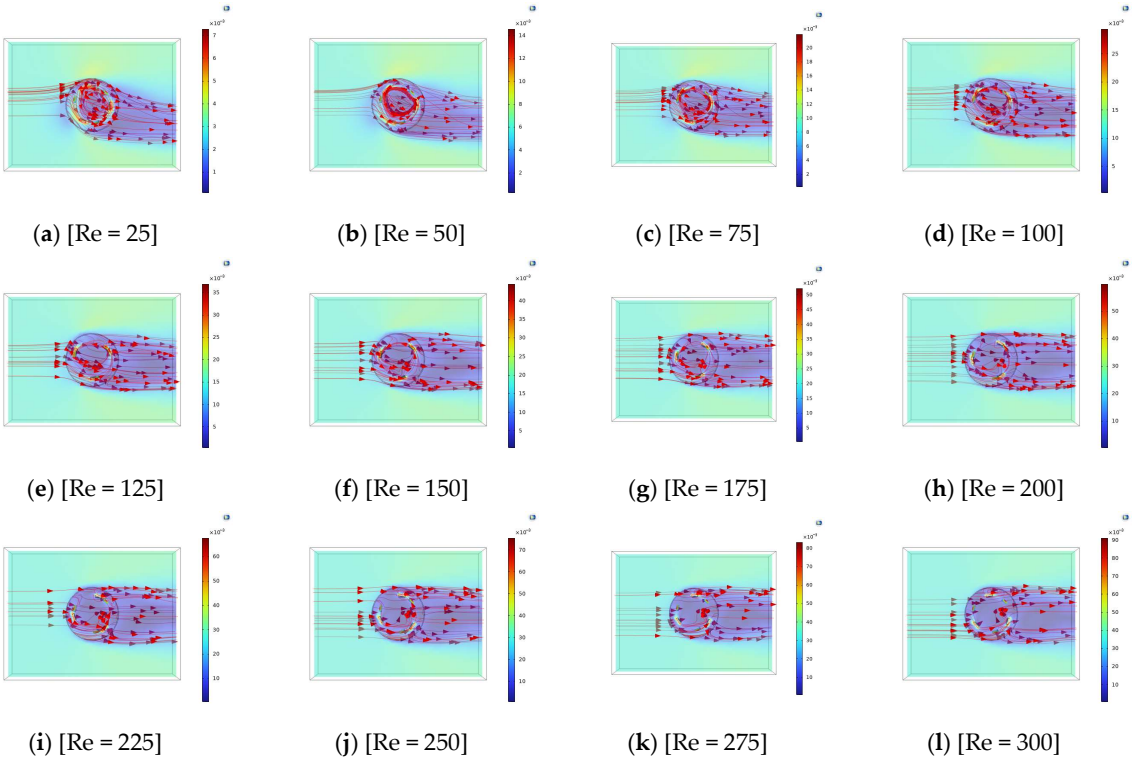
(**a**) [Re = 25] (**b**) [Re = 50] (**c**) [Re = 75] (**d**) [Re = 100]

(**e**) [Re = 125] (**f**) [Re = 150] (**g**) [Re = 175] (**h**) [Re = 200]

(**i**) [Re = 225] (**j**) [Re = 250] (**k**) [Re = 275] (**l**) [Re = 300]

Figure 2. Velocity magnitude contours and streamlines for blade model M1 (transformation depth RD = −50 mm) at Reynolds numbers of (**a**) 25, (**b**) 50, (**c**) 75, (**d**) 100, (**e**) 125, (**f**) 150, (**g**) 175, (**h**) 200, (**i**) 225, (**j**) 250, (**k**) 275, and (**l**) 300. The arrow represents velocity magnitude streamlines for blade model M1.

Model M2, characterized by moderately convex curvature (RD = −30 mm), shows a similar aerodynamic pattern but with subtle differences. At low Reynolds numbers, the flow attachment remained strong (Figure 3a), although the wake was marginally wider and less uniform than that of M1. Vortex shedding was initiated earlier at Re = 50 (Figure 3b), causing more pronounced wake oscillations as the Reynolds number increased. Despite this, the wake maintained reasonable coherence and flow stability across the Reynolds number range, supporting a relatively efficient aerodynamic behavior.



(**a**) [Re = 25] (**b**) [Re = 50] (**c**) [Re = 75] (**d**) [Re = 100]

(**e**) [Re = 125] (**f**) [Re = 150] (**g**) [Re = 175] (**h**) [Re = 200]

(**i**) [Re = 225] (**j**) [Re = 250] (**k**) [Re = 275] (**l**) [Re = 300]

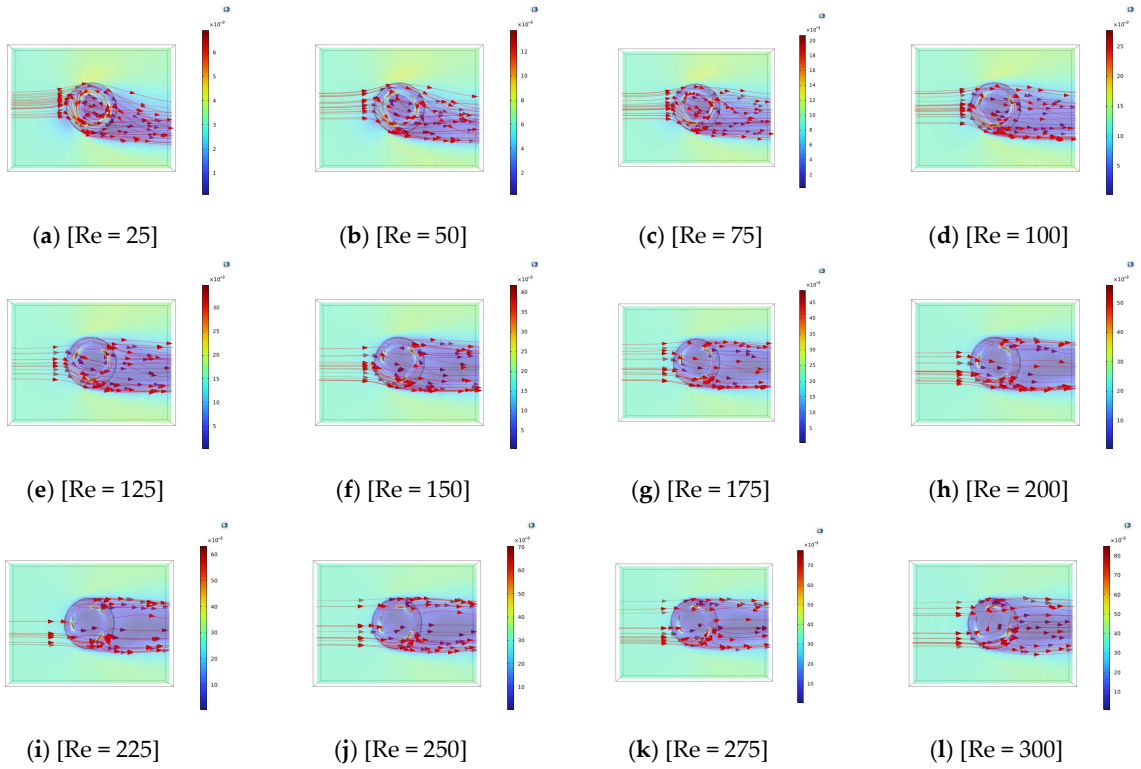
Figure 3. Velocity magnitude contours and streamlines for blade model M2 (transformation depth RD = −30 mm) at Reynolds numbers of (**a**) 25, (**b**) 50, (**c**) 75, (**d**) 100, (**e**) 125, (**f**) 150, (**g**) 175, (**h**) 200, (**i**) 225, (**j**) 250, (**k**) 275, and (**l**) 300.

Model M3, with near-neutral curvature (RD = −15 mm), began to show early signs of flow separation at Reynolds numbers greater than 100 (Figure 4d). The velocity contours revealed broader wake regions with increased turbulence, whereas the streamlines indicated intermittent detachment zones and recirculation bubbles downstream of the rotor (Figure 4e–l). These flow instabilities contributed to increased drag and reduced torque production compared to the more convex models.

The baseline concave blade, Model M4 (RD = 0 mm), showed substantial flow separation even at low Reynolds numbers (Re ≈ 50), as shown in Figure 5b. The wake widens and becomes irregular, featuring extensive low-velocity zones and turbulent vortex shedding downstream of the rotor (Figure 5c–l). These flow characteristics increase the aerodynamic drag and reduce the power extraction efficiency, confirming the inferior aerodynamic performance of the traditional concave design.

Model M5, with increased concavity (RD = +15 mm), exhibited pronounced flow detachment and highly diffused wakes across all Reynolds numbers. The velocity contours show large low-velocity zones near the blade surfaces and turbulent wake structures downstream (Figure 6a–l). This early and persistent flow separation leads to degraded aerodynamic performance and unstable torque generation.

Model M6, which had a stronger concavity (RD = +30 mm), experienced substantial flow separation at all Reynolds numbers. The wake turbulence was intense and irregular, with chaotic vortex shedding dominating the flow (Figure 7a–l). Broad velocity deficits near the blade surfaces caused significant aerodynamic losses, and unsteady wake dynamics induced fluctuating rotor loads.

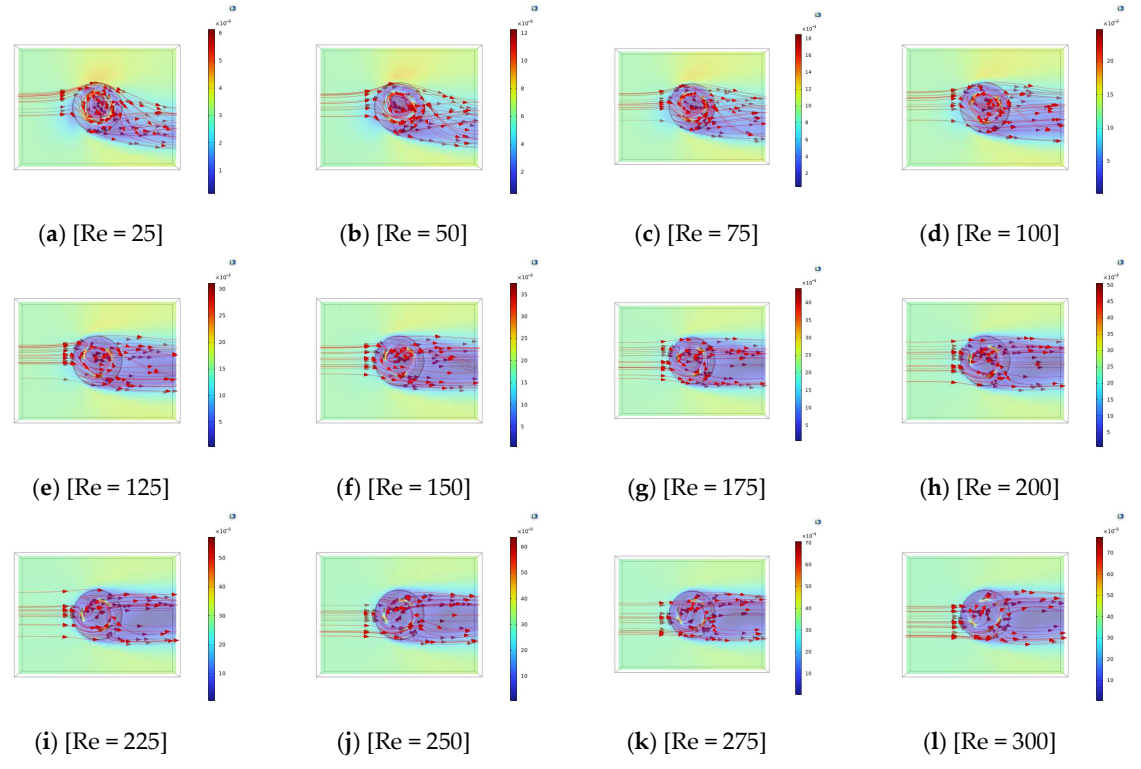


(**a**) [Re = 25] (**b**) [Re = 50] (**c**) [Re = 75] (**d**) [Re = 100]

(**e**) [Re = 125] (**f**) [Re = 150] (**g**) [Re = 175] (**h**) [Re = 200]

(**i**) [Re = 225] (**j**) [Re = 250] (**k**) [Re = 275] (**l**) [Re = 300]

Figure 4. Velocity magnitude contours and streamlines for blade model M3 (transformation depth RD = −15 mm) at Reynolds numbers of (**a**) 25, (**b**) 50, (**c**) 75, (**d**) 100, (**e**) 125, (**f**) 150, (**g**) 175, (**h**) 200, (**i**) 225, (**j**) 250, (**k**) 275, and (**l**) 300.

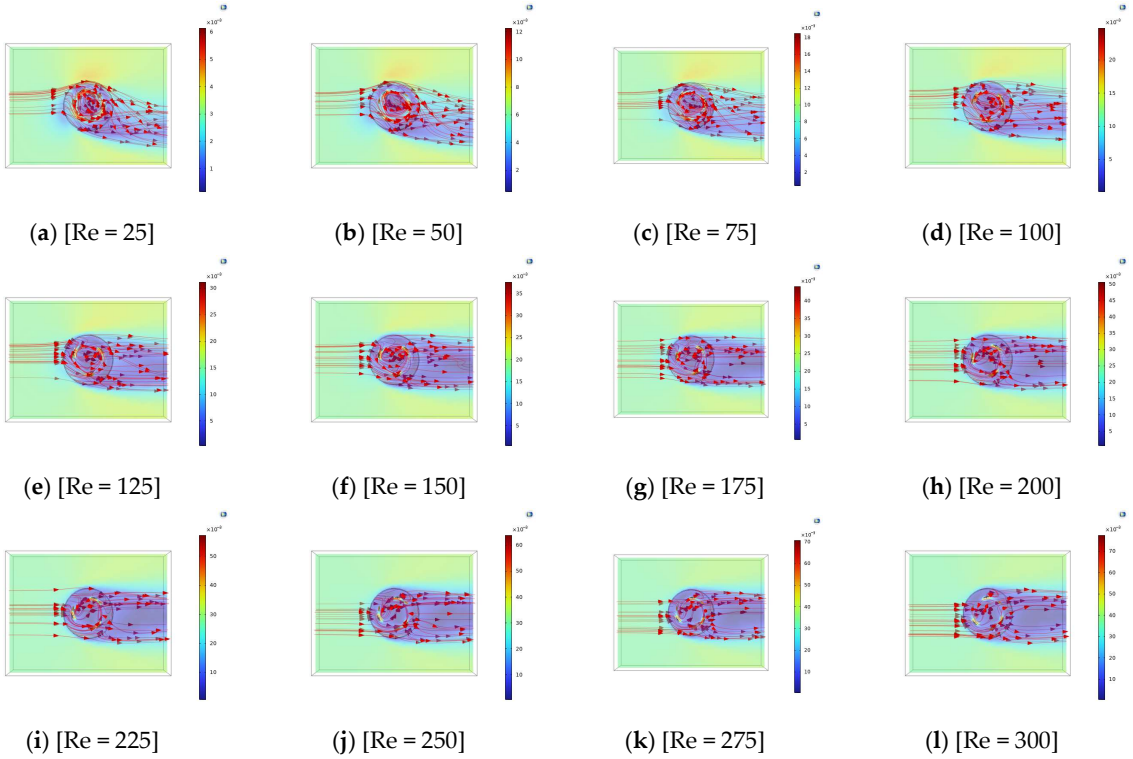


(**a**) [Re = 25] (**b**) [Re = 50] (**c**) [Re = 75] (**d**) [Re = 100]

(**e**) [Re = 125] (**f**) [Re = 150] (**g**) [Re = 175] (**h**) [Re = 200]

(**i**) [Re = 225] (**j**) [Re = 250] (**k**) [Re = 275] (**l**) [Re = 300]

Figure 5. Velocity magnitude contours and streamlines for blade model M4 (transformation depth RD = 0 mm) at Reynolds numbers of (**a**) 25, (**b**) 50, (**c**) 75, (**d**) 100, (**e**) 125, (**f**) 150, (**g**) 175, (**h**) 200, (**i**) 225, (**j**) 250, (**k**) 275, and (**l**) 300.

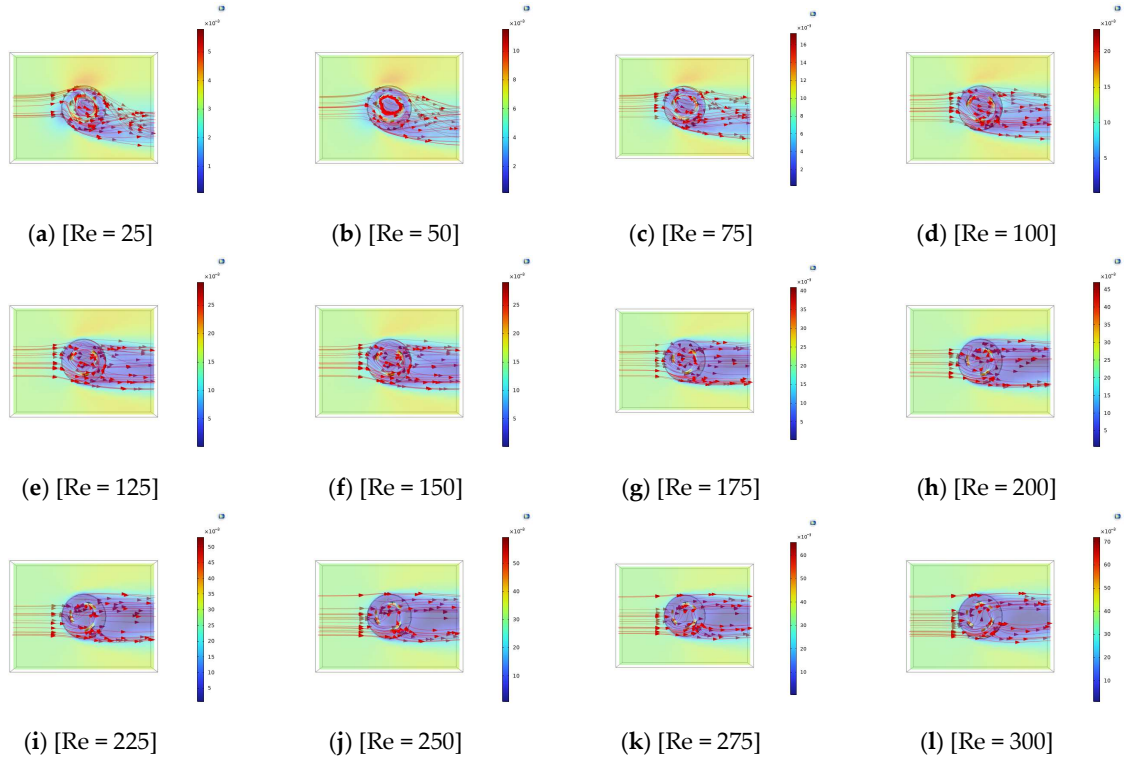


(**a**) [Re = 25] (**b**) [Re = 50] (**c**) [Re = 75] (**d**) [Re = 100]

(**e**) [Re = 125] (**f**) [Re = 150] (**g**) [Re = 175] (**h**) [Re = 200]

(**i**) [Re = 225] (**j**) [Re = 250] (**k**) [Re = 275] (**l**) [Re = 300]

Figure 6. Velocity magnitude contours and streamlines for blade model M5 (transformation depth RD = +15 mm) at Reynolds numbers of (**a**) 25, (**b**) 50, (**c**) 75, (**d**) 100, (**e**) 125, (**f**) 150, (**g**) 175, (**h**) 200, (**i**) 225, (**j**) 250, (**k**) 275, and (**l**) 300.



(**a**) [Re = 25] (**b**) [Re = 50] (**c**) [Re = 75] (**d**) [Re = 100]

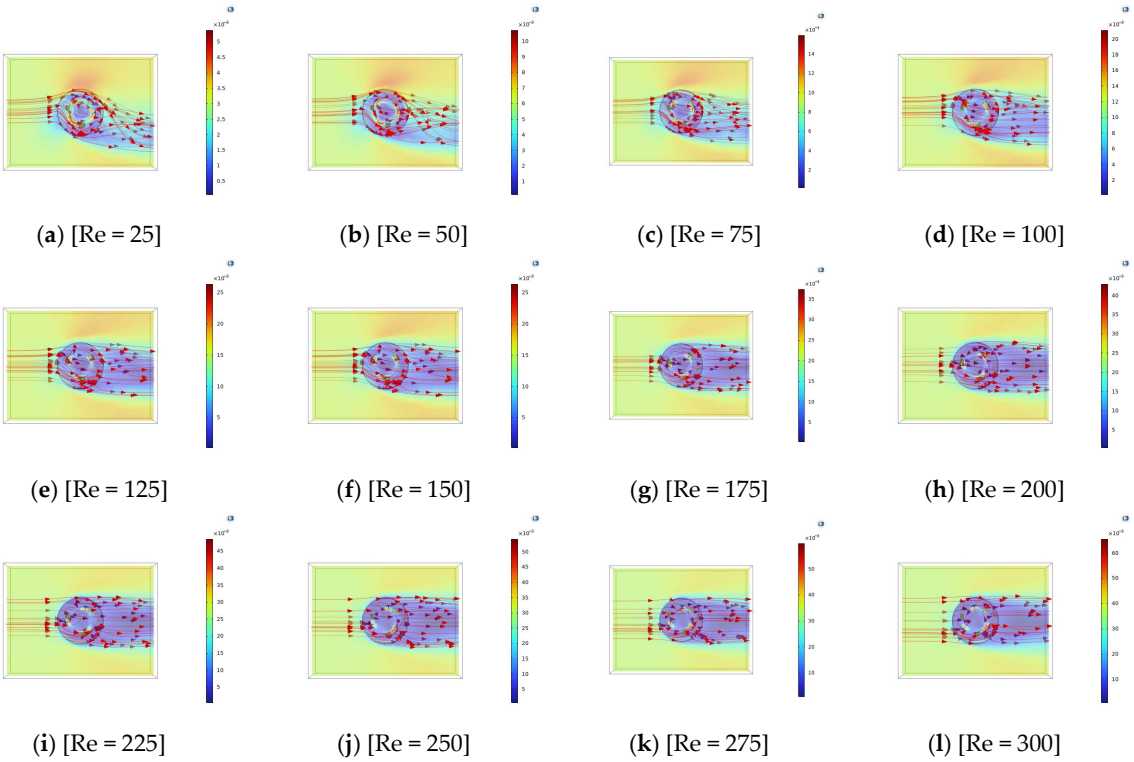
(**e**) [Re = 125] (**f**) [Re = 150] (**g**) [Re = 175] (**h**) [Re = 200]

(**i**) [Re = 225] (**j**) [Re = 250] (**k**) [Re = 275] (**l**) [Re = 300]

Figure 7. Velocity magnitude contours and streamlines for blade model M6 (transformation depth RD = +30 mm) at Reynolds numbers of (**a**) 25, (**b**) 50, (**c**) 75, (**d**) 100, (**e**) 125, (**f**) 150, (**g**) 175, (**h**) 200, (**i**) 225, (**j**) 250, (**k**) 275, and (**l**) 300.

The most concave blade, model M7 (RD = +50 mm), exhibited the poorest flow characteristics. The velocity contours indicate extensive flow separation and diffuse turbulent

wakes, even at the lowest Reynolds numbers (Figure 8a), which worsened significantly at higher Reynolds numbers (Figure 8b–l). Large recirculation zones and unstable flow attachment result in substantial aerodynamic inefficiencies in the flow.



(**a**) [Re = 25] (**b**) [Re = 50] (**c**) [Re = 75] (**d**) [Re = 100]

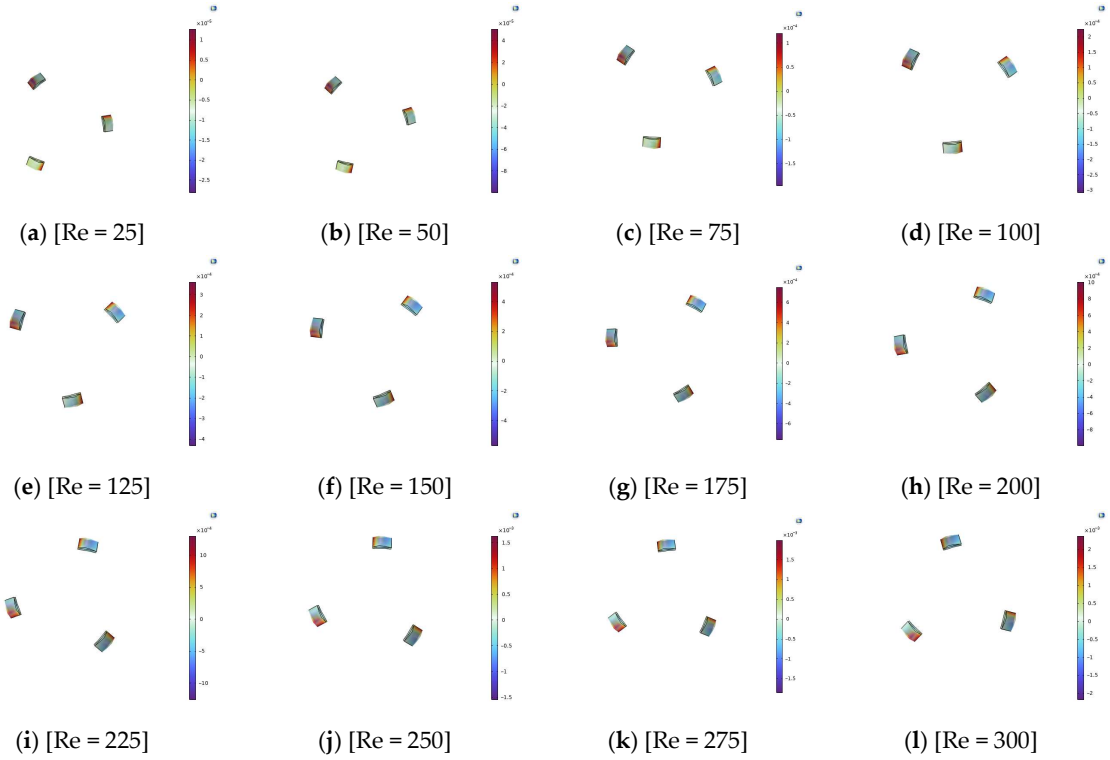
(**e**) [Re = 125] (**f**) [Re = 150] (**g**) [Re = 175] (**h**) [Re = 200]

(**i**) [Re = 225] (**j**) [Re = 250] (**k**) [Re = 275] (**l**) [Re = 300]

Figure 8. Velocity magnitude contours and streamlines for blade model M7 (transformation depth RD = +50 mm) at Reynolds numbers of (**a**) 25, (**b**) 50, (**c**) 75, (**d**) 100, (**e**) 125, (**f**) 150, (**g**) 175, (**h**) 200, (**i**) 225, (**j**) 250, (**k**) 275, and (**l**) 300.

3.2. Pressure Field Analysis

The pressure distribution over wind turbine blades is a fundamental determinant of aerodynamic performance, directly influencing the lift generation, drag forces, and flow stability. The CFD simulations in the present study revealed clear distinctions in the pressure fields among the blade configurations with varying curvatures (transformation depth RD) and Reynolds numbers ranging from 25 to 300. Understanding these pressure dynamics is essential for explaining the variations in the power extraction efficiency and flow behaviors observed in the velocity fields. Model M1 (deeply convex, RD = −50 mm) consistently shows the most favorable pressure characteristics throughout the Reynolds number range. At Re = 25, the pressure field (Figure 9a) illustrates a pronounced suction zone on the leeward (downwind) side of the blade, with the pressure dropping to values near −1.5, whereas the windward side maintains an elevated pressure, establishing a strong pressure differential essential for lift generation. This distribution promotes stable flow attachment and minimizes adverse pressure gradients that can trigger early separation. As the Reynolds number increased, the pressure gradients maintained their strength and uniformity (Figure 9b–l), indicating that the convex geometry robustly supported the aerodynamic loading, even under increased inertial forces. The consistently high suction pressure and smooth pressure transitions reduced drag and contributed to the narrow, coherent wakes observed in the velocity analyses.



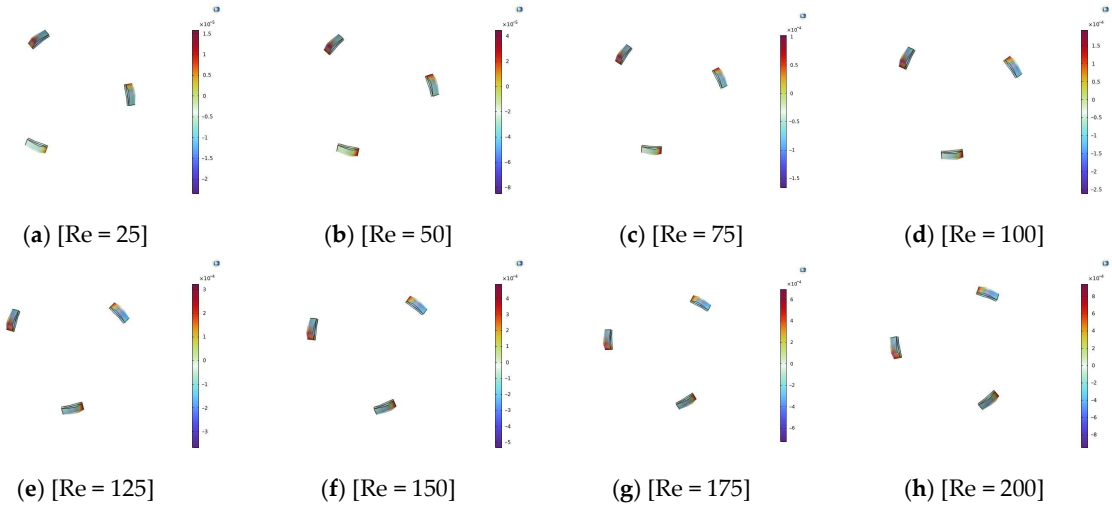
(**a**) [Re = 25] (**b**) [Re = 50] (**c**) [Re = 75] (**d**) [Re = 100]

(**e**) [Re = 125] (**f**) [Re = 150] (**g**) [Re = 175] (**h**) [Re = 200]

(**i**) [Re = 225] (**j**) [Re = 250] (**k**) [Re = 275] (**l**) [Re = 300]

Figure 9. Pressure distribution contours for blade model M1 (RD = −50 mm) at Reynolds numbers of (**a**) 25, (**b**) 50, (**c**) 75, (**d**) 100, (**e**) 125, (**f**) 150, (**g**) 175, (**h**) 200, (**i**) 225, (**j**) 250, (**k**) 275, and (**l**) 300.

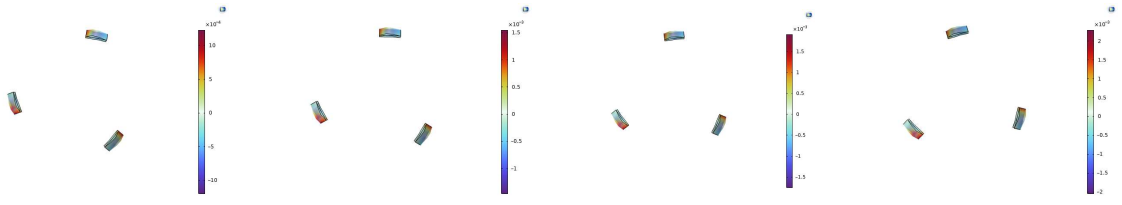
Model M2 (RD = −30 mm) similarly benefits from beneficial pressure gradients, although the magnitude of the suction zone on the leeward side is slightly reduced compared to M1 (Figure 10a). Despite this reduction, the pressure distribution remained sufficiently favorable to generate effective lift and sustain the attached flow over the blade surfaces. As the Reynolds number increased, the pressure differential gradually decreased but remained sufficiently balanced to prevent a significant flow separation (Figure 10b–l). The pressure fields correlated well with the velocity streamlines, showing coherent wakes and stable flow patterns, thereby supporting the aerodynamic efficiency of the moderately convex shape of the head.



(**a**) [Re = 25] (**b**) [Re = 50] (**c**) [Re = 75] (**d**) [Re = 100]

(**e**) [Re = 125] (**f**) [Re = 150] (**g**) [Re = 175] (**h**) [Re = 200]

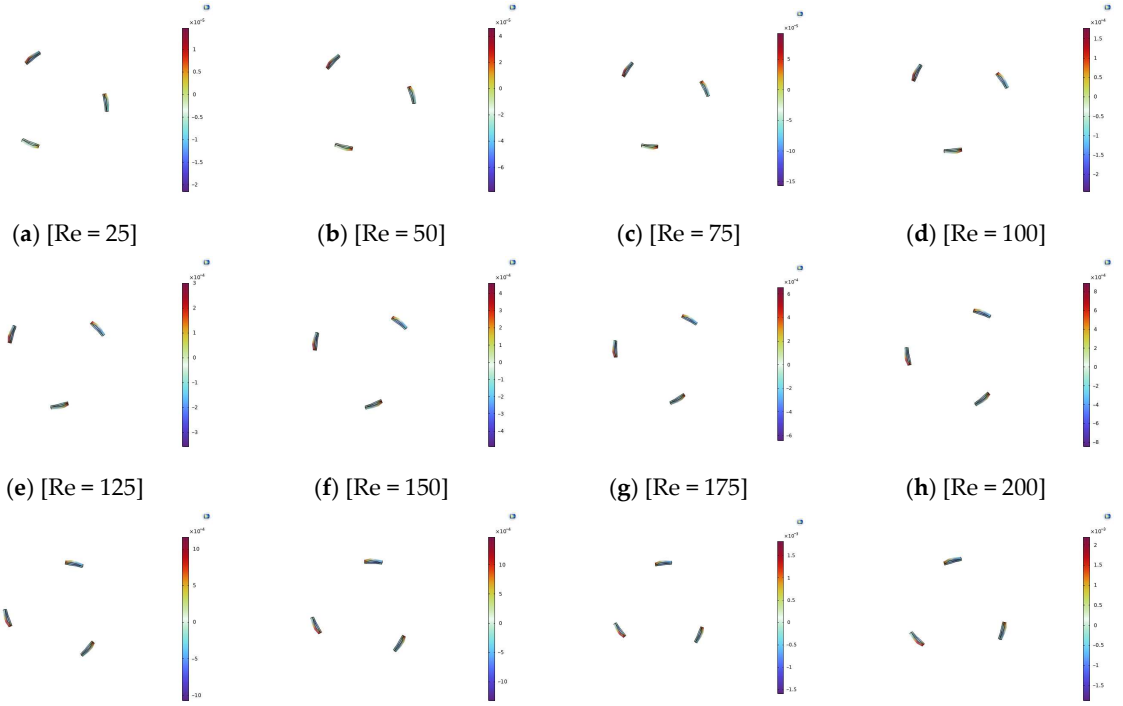
Figure 10. *Cont.*



(**i**) [Re = 225] (**j**) [Re = 250] (**k**) [Re = 275] (**l**) [Re = 300]

Figure 10. Pressure distribution contours for blade model M2 (RD = −30 mm) at Reynolds numbers of (**a**) 25, (**b**) 50, (**c**) 75, (**d**) 100, (**e**) 125, (**f**) 150, (**g**) 175, (**h**) 200, (**i**) 225, (**j**) 250, (**k**) 275, and (**l**) 300.

Moving toward near-neutral curvature, model M3 (RD = −15 mm) shows notable changes in pressure behavior. At low Reynolds numbers, the pressure distributions maintained a basic differential conducive to lift, but the suction region weakened and became less extensive (Figure 11a). With increasing Reynolds number, the pressure gradients deteriorated markedly (Figure 11b–l), with larger zones of high pressure developing on the windward side and a reduced suction on the leeward side. These factors promote an earlier onset of flow separation, as evidenced by the increasing size of the stagnation regions and adverse gradients, which negatively impact the lift-to-drag ratio. This deterioration aligns with the observed broadening of the turbulent wakes and loss of flow coherence in the velocity analyses.



(**a**) [Re = 25] (**b**) [Re = 50] (**c**) [Re = 75] (**d**) [Re = 100]

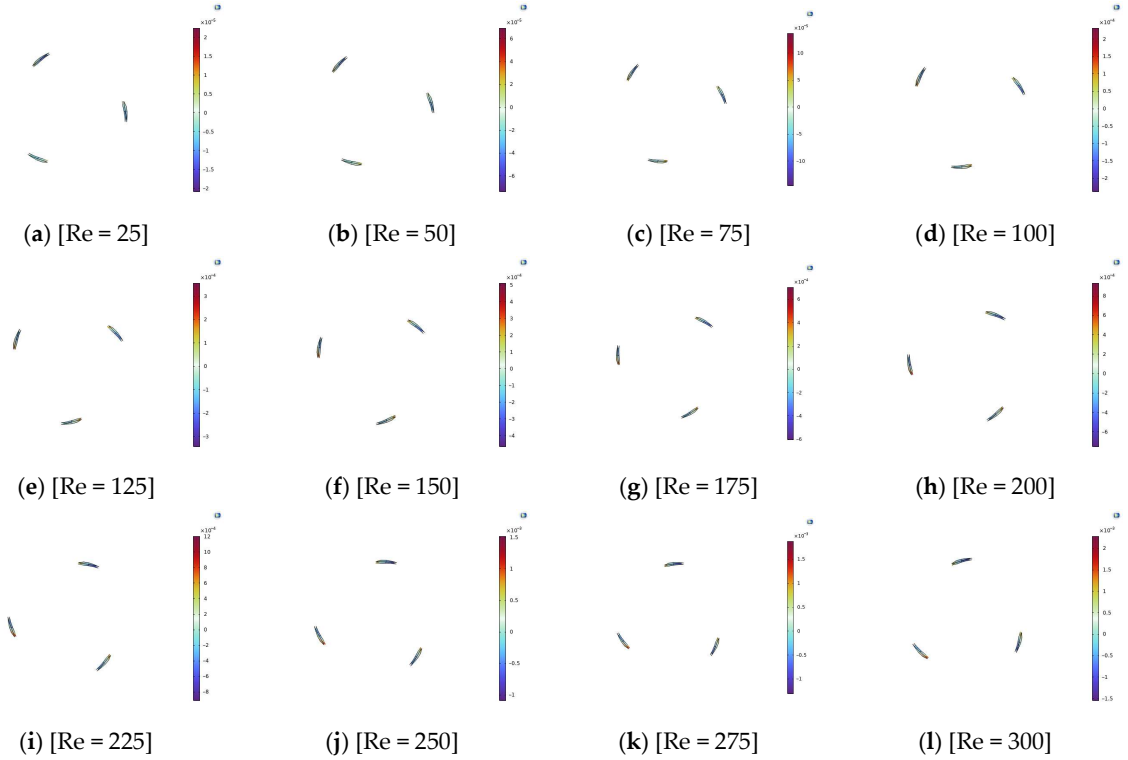
(**e**) [Re = 125] (**f**) [Re = 150] (**g**) [Re = 175] (**h**) [Re = 200]

(**i**) [Re = 225] (**j**) [Re = 250] (**k**) [Re = 275] (**l**) [Re = 300]

Figure 11. Pressure distribution contours for blade model M3 (RD = −15 mm) at Reynolds numbers of (**a**) 25, (**b**) 50, (**c**) 75, (**d**) 100, (**e**) 125, (**f**) 150, (**g**) 175, (**h**) 200, (**i**) 225, (**j**) 250, (**k**) 275, and (**l**) 300.

The baseline concave blade model M4 (RD = 0 mm) showed a further decline in the pressure distribution quality. Even at relatively low Reynolds numbers (Re = 50, Figure 12b), the pressure field exhibits large stagnation areas with diminished pressure differentials, which significantly restricts lift production. As the Reynolds number increased, the pressure contours became highly irregular and scattered (Figure 12c–l), with prominent adverse gradients and separated-flow regions. These characteristics contribute to the

strong turbulent wakes and broad velocity deficits observed in the velocity field, resulting in increased aerodynamic drag and low power extraction efficiency. Pressure-induced flow separation is a key factor underlying the inferior performance of traditional concave blade designs.



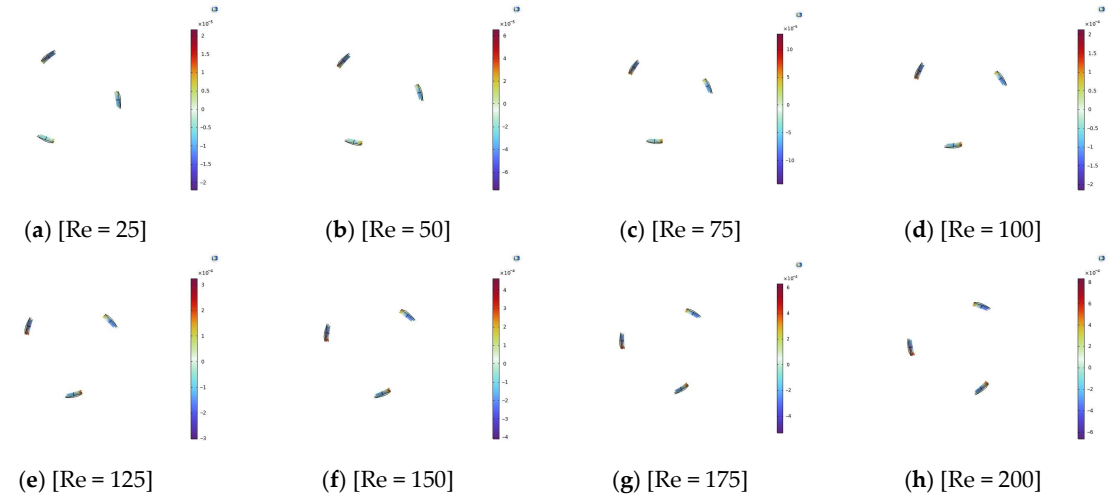
(**a**) [Re = 25] (**b**) [Re = 50] (**c**) [Re = 75] (**d**) [Re = 100]

(**e**) [Re = 125] (**f**) [Re = 150] (**g**) [Re = 175] (**h**) [Re = 200]

(**i**) [Re = 225] (**j**) [Re = 250] (**k**) [Re = 275] (**l**) [Re = 300]

Figure 12. Pressure distribution contours for blade model M4 (RD = 0 mm) at Reynolds numbers of (**a**) 25, (**b**) 50, (**c**) 75, (**d**) 100, (**e**) 125, (**f**) 150, (**g**) 175, (**h**) 200, (**i**) 225, (**j**) 250, (**k**) 275, and (**l**) 300.

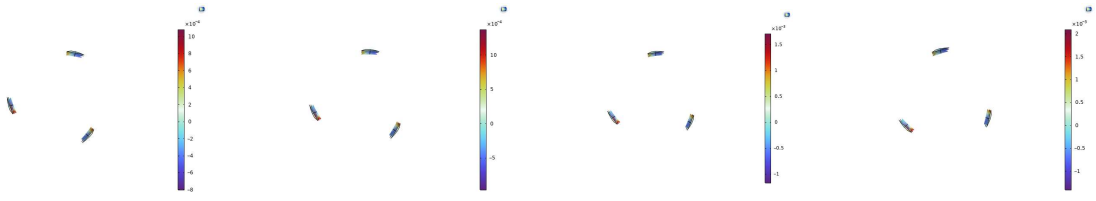
By increasing the concavity further, model M5 (RD = +15 mm) presents extensive regions of high stagnation pressure on the windward blade surfaces coupled with significantly reduced suction on the leeward sides (Figure 13a–l). These adverse pressure patterns intensified the flow separation and promoted early detachment across the Reynolds numbers. The pressure contours became increasingly nonuniform with increasing Re, indicating flow instability and turbulent wake formation, which severely degraded the lift production and torque consistency.



(**a**) [Re = 25] (**b**) [Re = 50] (**c**) [Re = 75] (**d**) [Re = 100]

(**e**) [Re = 125] (**f**) [Re = 150] (**g**) [Re = 175] (**h**) [Re = 200]

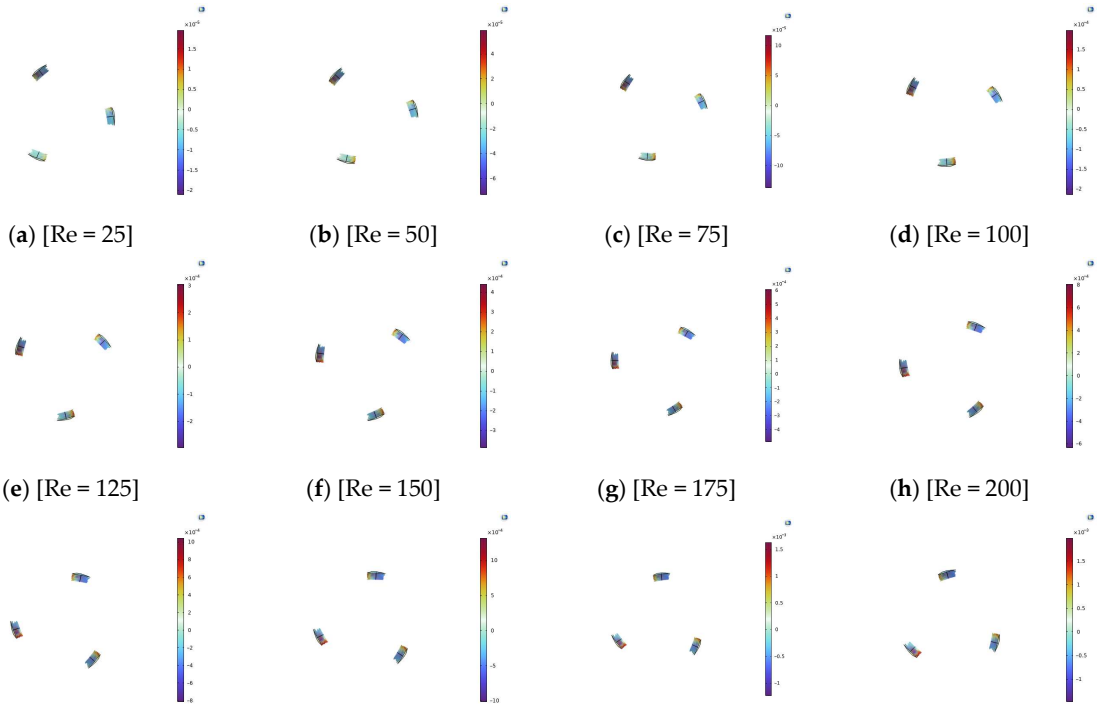
Figure 13. *Cont.*



(**i**) [Re = 225] (**j**) [Re = 250] (**k**) [Re = 275] (**l**) [Re = 300]

Figure 13. Pressure distribution contours for blade model M5 (RD = +15 mm) at Reynolds numbers of (**a**) 25, (**b**) 50, (**c**) 75, (**d**) 100, (**e**) 125, (**f**) 150, (**g**) 175, (**h**) 200, (**i**) 225, (**j**) 250, (**k**) 275, and (**l**) 300.

The effect intensified in model M6 (RD = +30 mm), where the pressure differentials were largely unfavorable for aerodynamic performance. The leeward low pressure regions shrink drastically, whereas the windward high pressure zones dominated the blade surface (Figure 14a–l). This imbalance corresponds to the very strong flow separation and turbulent wake formation observed in the velocity results, which significantly increased the drag forces and reduced the overall turbine efficiency.



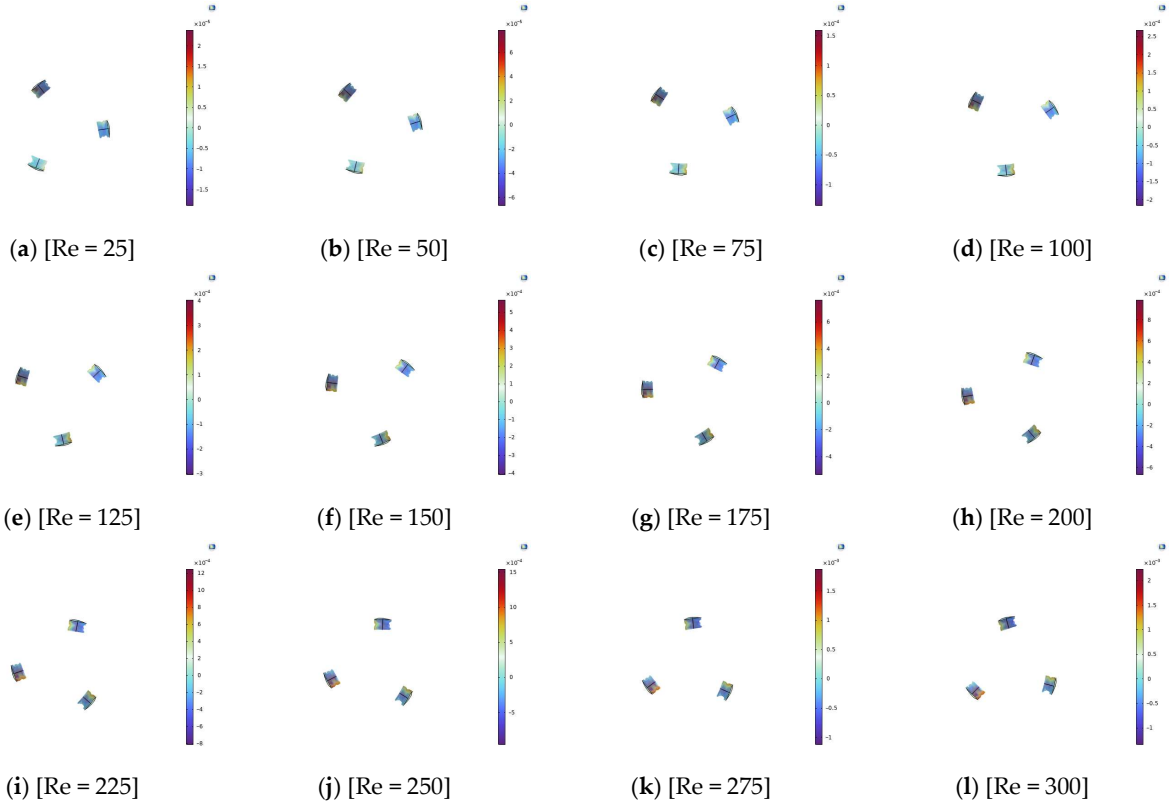
(**a**) [Re = 25] (**b**) [Re = 50] (**c**) [Re = 75] (**d**) [Re = 100]

(**e**) [Re = 125] (**f**) [Re = 150] (**g**) [Re = 175] (**h**) [Re = 200]

(**i**) [Re = 225] (**j**) [Re = 250] (**k**) [Re = 275] (**l**) [Re = 300]

Figure 14. Pressure distribution contours for blade model M6 (RD = +30 mm) at Reynolds numbers of (**a**) 25, (**b**) 50, (**c**) 75, (**d**) 100, (**e**) 125, (**f**) 150, (**g**) 175, (**h**) 200, (**i**) 225, (**j**) 250, (**k**) 275, and (**l**) 300.

Finally, model M7, which had the most concave curvature (RD = +50 mm), exhibited the poorest pressure distribution quality. The pressure contours at all Reynolds numbers (Figure 15a–l) revealed highly irregular fields characterized by minimal suction on the leeward side and strong stagnation points on the windward side. This led to maximal flow separation, unstable wakes, and highly inefficient lift generation, confirming the unsuitability of this configuration for effective energy harvesting under low-speed wind conditions.



(**a**) [Re = 25] (**b**) [Re = 50] (**c**) [Re = 75] (**d**) [Re = 100]

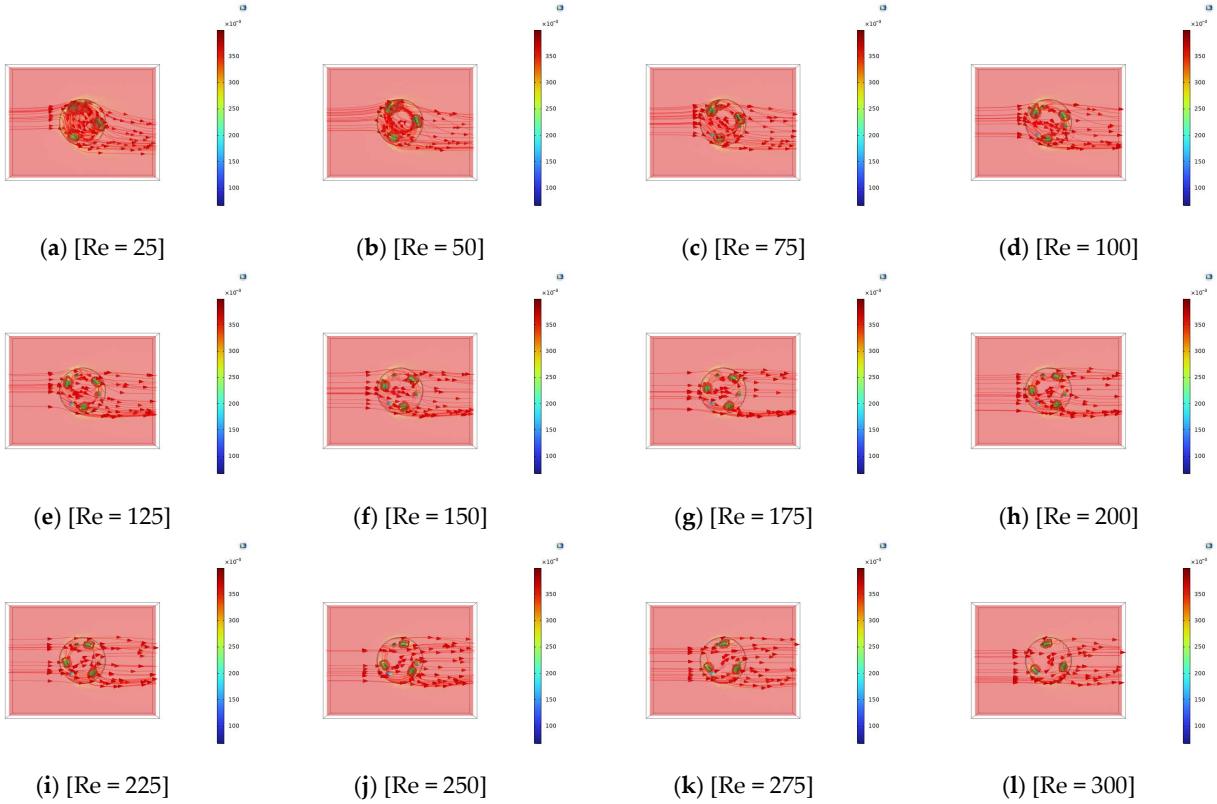
(**e**) [Re = 125] (**f**) [Re = 150] (**g**) [Re = 175] (**h**) [Re = 200]

(**i**) [Re = 225] (**j**) [Re = 250] (**k**) [Re = 275] (**l**) [Re = 300]

Figure 15. Pressure distribution contours for blade model M7 (RD = +50 mm) at Reynolds numbers of (**a**) 25, (**b**) 50, (**c**) 75, (**d**) 100, (**e**) 125, (**f**) 150, (**g**) 175, (**h**) 200, (**i**) 225, (**j**) 250, (**k**) 275, and (**l**) 300.

3.3. Vorticity and Rotational Performance

Vorticity, a measure of local fluid rotation, is a fundamental indicator of wake dynamics, energy transfer, and flow stability in vertical axis wind turbines (VAWTs). The spatial and temporal distributions of vorticity directly influence the ability of the turbine to convert aerodynamic forces into mechanical torque, thereby affecting the power output and structural loading. The current numerical investigation evaluated how blade curvature, quantified by the transformation depth (RD), modulates vorticity generation and organization across a Reynolds number spectrum from 25 to 300, which is representative of small-scale, low-speed wind environments. Model M1, characterized by deeply convex blades (RD = −50 mm), exhibits robust and well-organized vortical structures at all Reynolds numbers. At the lowest Reynolds number (Re = 25), the vorticity contours (Figure 16a) revealed strong coherent vortex shedding localized near the blade surfaces, indicating efficient angular momentum transfer and minimal turbulent diffusion. This coherence supports a smooth aerodynamic loading cycle, which reduces flow-induced vibrations and enhances structural durability. As the Reynolds number increased, the vorticity magnitude intensified steadily (Figure 16b–l), reflecting the augmented inertial forces and strengthened aerodynamic lift. The wake remained compact, with vortices maintaining stable shedding frequencies, which minimized energy losses due to turbulence and optimized the conversion of fluid kinetic energy into the rotational torque. This stability corroborates the superior torque coefficients and power coefficients obtained for M1 in the performance analyses, underscoring the aerodynamic benefits of the deep convex curvature in low Reynolds number regimes.



(**a**) [Re = 25] (**b**) [Re = 50] (**c**) [Re = 75] (**d**) [Re = 100]

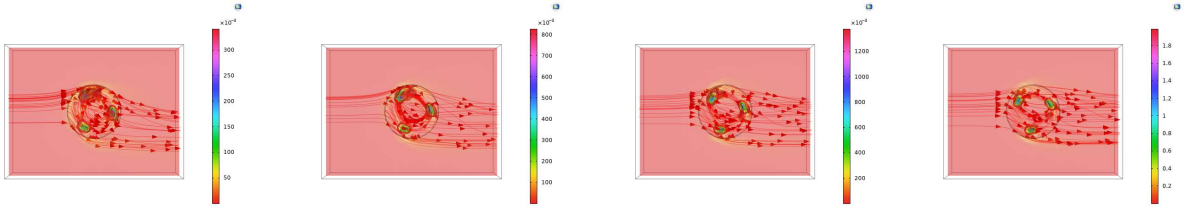
(**e**) [Re = 125] (**f**) [Re = 150] (**g**) [Re = 175] (**h**) [Re = 200]

(**i**) [Re = 225] (**j**) [Re = 250] (**k**) [Re = 275] (**l**) [Re = 300]

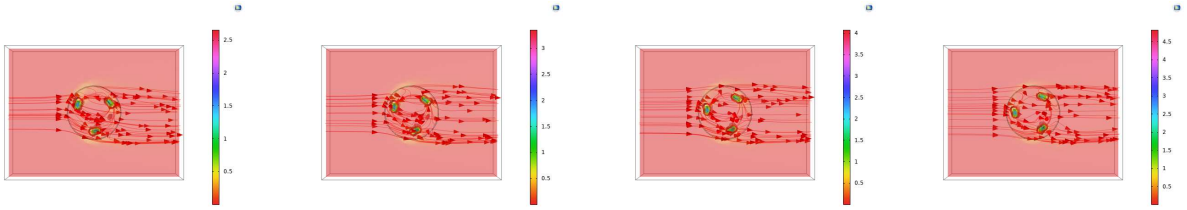
Figure 16. Vorticity contours and streamlines for blade model M1 (RD = −50 mm) at various Reynolds numbers: (**a**) 25, (**b**) 50, (**c**) 75, (**d**) 100, (**e**) 125, (**f**) 150, (**g**) 175, (**h**) 200, (**i**) 225, (**j**) 250, (**k**) 275, and (**l**) 300.

For model M2 (RD = −30 mm), the vortical structures remained well-defined but exhibited slightly lower peak magnitudes than those of M1, particularly at lower Reynolds numbers (Figure 17a). This suggests a minor decrease in aerodynamic loading but retains sufficient coherence for stable torque production. As the Reynolds number increased, the wake vortices experienced moderate interaction and broadening (Figure 17b–l), reflecting a slight increase in turbulence intensity. Despite this, vortex shedding maintained relatively consistent spatial and temporal characteristics, supporting an aerodynamic performance that was superior to that of less convex geometries. The maintenance of coherent vortices at moderate Reynolds numbers implies a stable aerodynamic environment conducive to sustained power output and reduced mechanical fatigue.

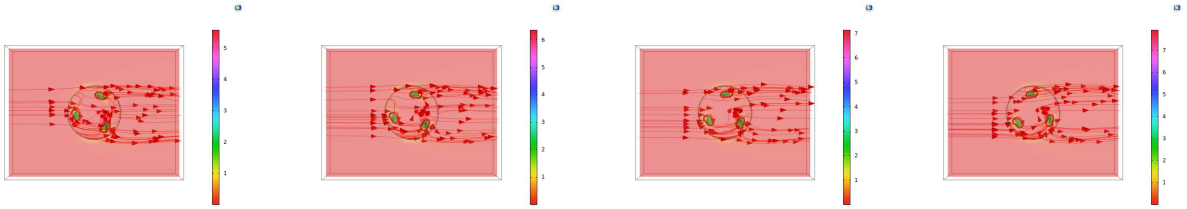
Approaching neutral curvature, model M3 (RD = −15 mm) demonstrated a clear reduction in vorticity magnitude and coherence across the Reynolds number range. At low Reynolds numbers, the vortices remained somewhat organized but weaker in intensity (Figure 18a), indicating a less efficient momentum exchange. As the flow velocity increased, the vortical structures became fragmented and spatially dispersed (Figure 18b–l), indicating enhanced turbulence and vortex breakdown. These effects result in fluctuating aerodynamic forces on the blades, causing unstable torque generation and potentially increasing structural fatigue. The loss of vortex coherence with a curvature approaching neutrality highlights the aerodynamic penalty incurred when deviating from convex blade geometries under laminar-to-transitional flow regimes.



(**a**) [Re = 25] (**b**) [Re = 50] (**c**) [Re = 75] (**d**) [Re = 100]

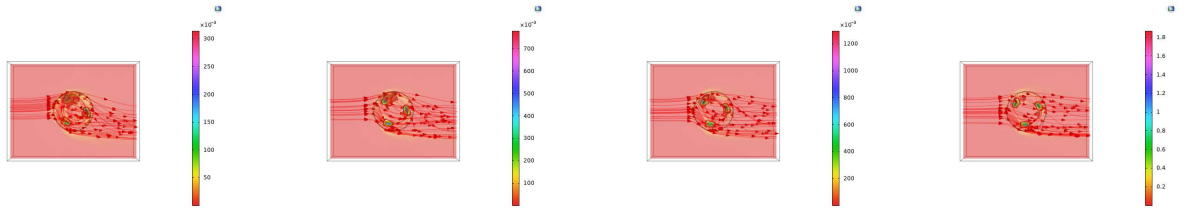


(**e**) [Re = 125] (**f**) [Re = 150] (**g**) [Re = 175] (**h**) [Re = 200]

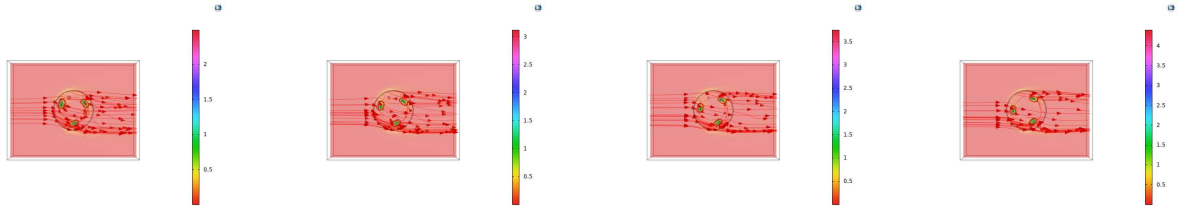


(**i**) [Re = 225] (**j**) [Re = 250] (**k**) [Re = 275] (**l**) [Re = 300]

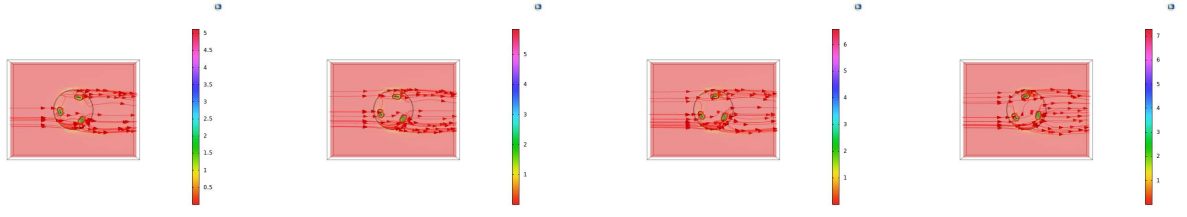
Figure 17. Vorticity contours and streamlines for blade model M2 (RD = −30 mm) at Reynolds number (**a**) 25, (**b**) 50, (**c**) 75, (**d**) 100, (**e**) 125, (**f**) 150, (**g**) 175, (**h**) 200, (**i**) 225, (**j**) 250, (**k**) 275, (**l**) 300.



(**a**) [Re = 25] (**b**) [Re = 50] (**c**) [Re = 75] (**d**) [Re = 100]



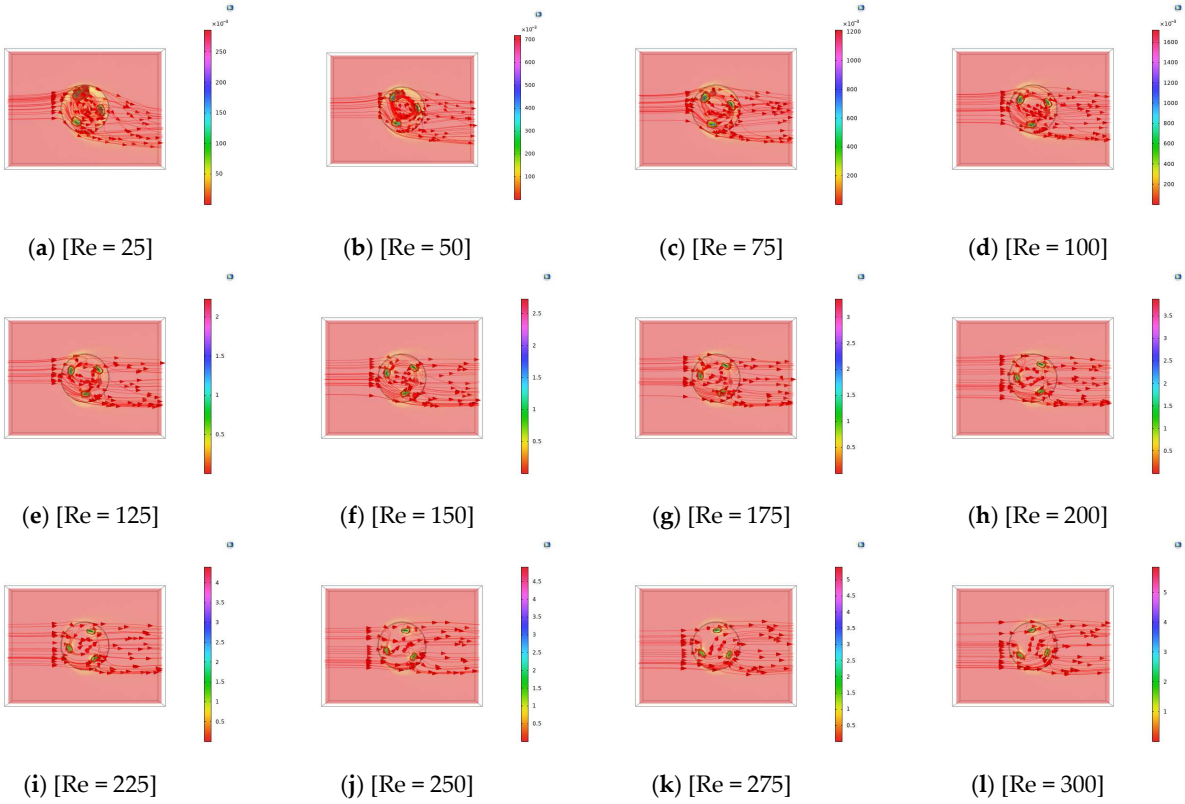
(**e**) [Re = 125] (**f**) [Re = 150] (**g**) [Re = 175] (**h**) [Re = 200]



(**i**) [Re = 225] (**j**) [Re = 250] (**k**) [Re = 275] (**l**) [Re = 300]

Figure 18. Vorticity contours and streamlines for blade model M3 (RD = −15 mm) at Reynolds number (**a**) 25, (**b**) 50, (**c**) 75, (**d**) 100, (**e**) 125, (**f**) 150, (**g**) 175, (**h**) 200, (**i**) 225, (**j**) 250, (**k**) 275, (**l**) 300.

The baseline model M4 (concave blades, RD = 0 mm) experiences moderate vorticity magnitudes at low Reynolds numbers but displays highly irregular and chaotic vortex shedding beyond Re = 50 (Figure 19a–l). These unsteady vortical flows contribute to fluctuating aerodynamic loads and diminish torque consistency, thereby increasing the risk of fatigue. The irregular wake topology disrupts the smooth transfer of angular momentum, thereby lowering the energy conversion efficiency of the turbines. Such turbulent wake conditions correspond to the broad velocity deficits and unstable flow attachments observed in the velocity and pressure analyses, underscoring the limitations of the concave blade design under low-speed wind conditions.



(**a**) [Re = 25] (**b**) [Re = 50] (**c**) [Re = 75] (**d**) [Re = 100]

(**e**) [Re = 125] (**f**) [Re = 150] (**g**) [Re = 175] (**h**) [Re = 200]

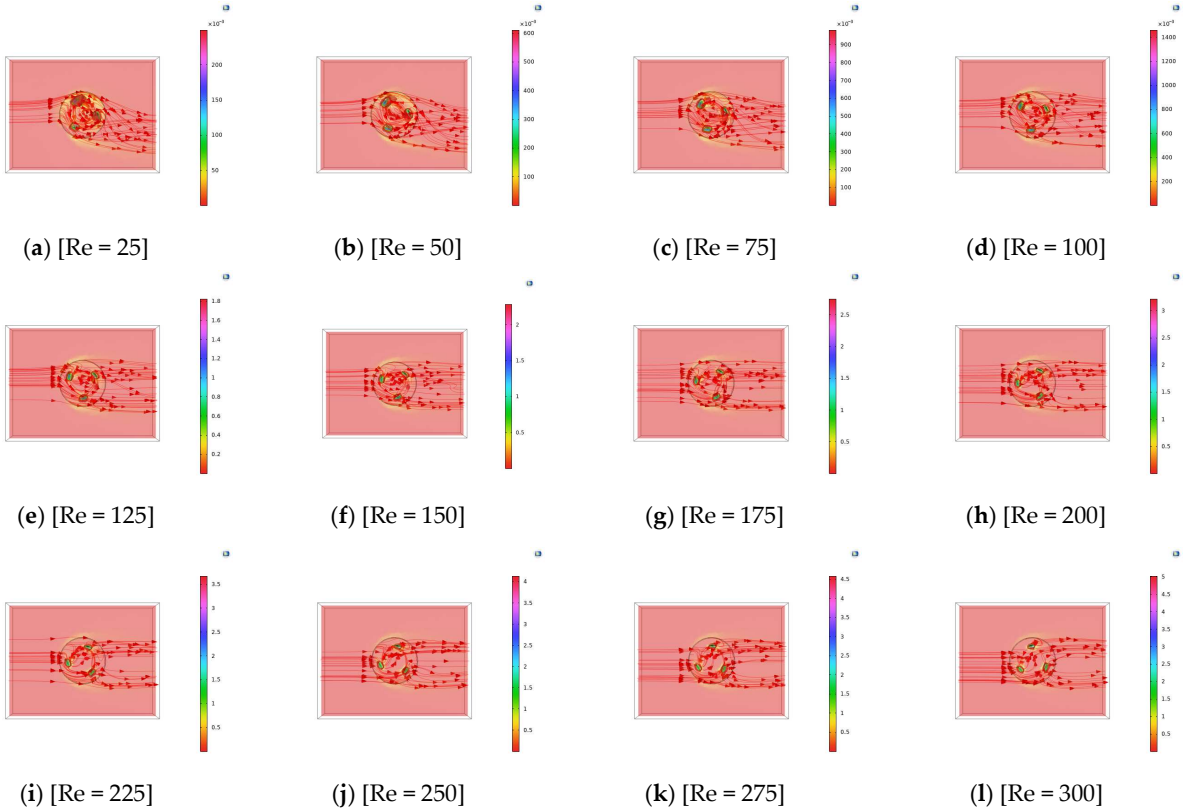
(**i**) [Re = 225] (**j**) [Re = 250] (**k**) [Re = 275] (**l**) [Re = 300]

Figure 19. Vorticity contours and streamlines for blade model M4 (RD = 0 mm) at various Reynolds numbers: (**a**) 25, (**b**) 50, (**c**) 75, (**d**) 100, (**e**) 125, (**f**) 150, (**g**) 175, (**h**) 200, (**i**) 225, (**j**) 250, (**k**) 275, and (**l**) 300.

With increasing concavity, M5, M6, and M7 exhibited progressively weaker and more chaotic vorticity fields. Model M5 (RD = +15 mm) exhibited fragmented vortex structures and strong turbulent diffusion across all Reynolds numbers (Figure 20a–l), severely degrading the aerodynamic efficiency and torque output. The wake becomes diffuse, promoting enhanced energy dissipation and irregular loading of the rotors.

Model M6 (RD = +30 mm) experiences intensified turbulence and diminished coherent vortex structures, with vortices losing spatial organization and strength (Figure 21a–l). This results in highly unsteady aerodynamic forces and lower torque consistency, negatively impacting turbine reliability and performance under fluctuating wind conditions.

The most concave blade, model M7 (RD = +50 mm), exhibited the weakest and most chaotic vortical flows throughout the Reynolds number range (Figure 22a–l). Vortex breakdown and wake diffusion dominate, preventing effective torque generation and severely limiting aerodynamic efficiency. This unsteady flow regime translates into an unstable power output and elevated structural loading, rendering this blade shape the least favorable option.

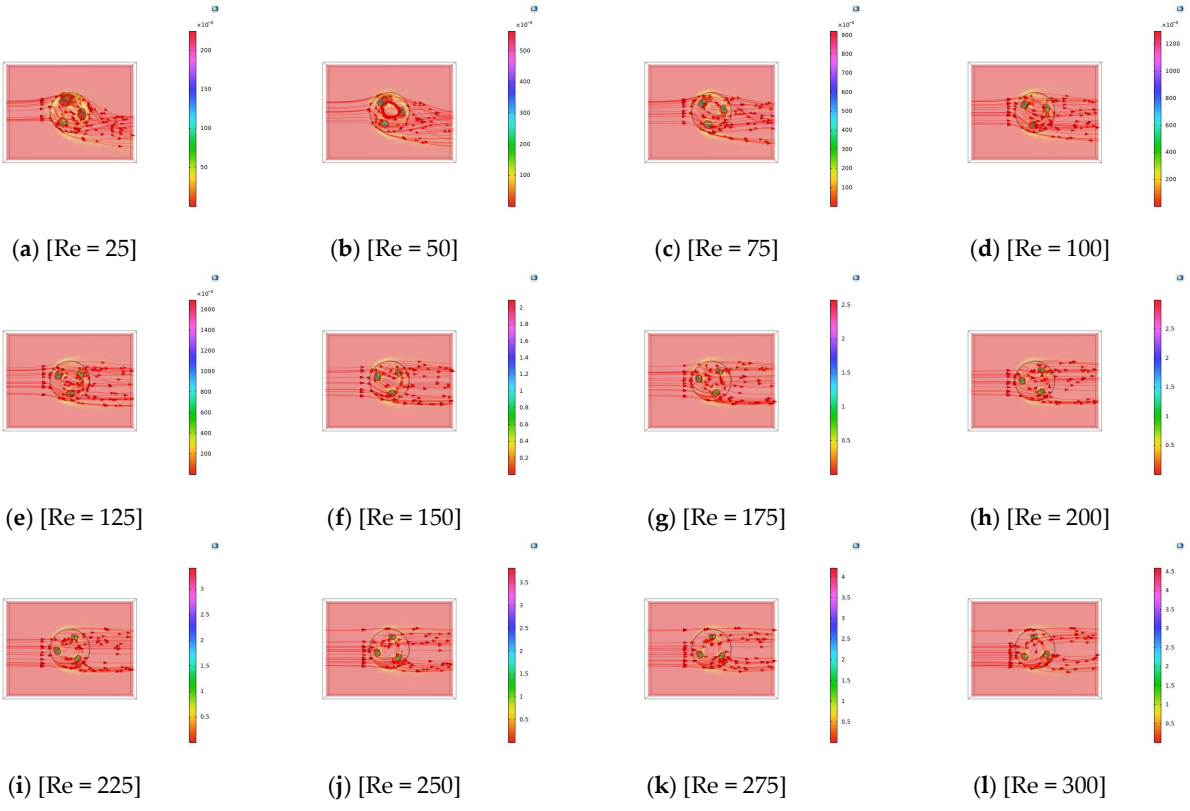


(**a**) [Re = 25] (**b**) [Re = 50] (**c**) [Re = 75] (**d**) [Re = 100]

(**e**) [Re = 125] (**f**) [Re = 150] (**g**) [Re = 175] (**h**) [Re = 200]

(**i**) [Re = 225] (**j**) [Re = 250] (**k**) [Re = 275] (**l**) [Re = 300]

Figure 20. Vorticity contours and streamlines for blade model M5 (RD = +15 mm) at various Reynolds numbers: (**a**) 25, (**b**) 50, (**c**) 75, (**d**) 100, (**e**) 125, (**f**) 150, (**g**) 175, (**h**) 200, (**i**) 225, (**j**) 250, (**k**) 275, and (**l**) 300.

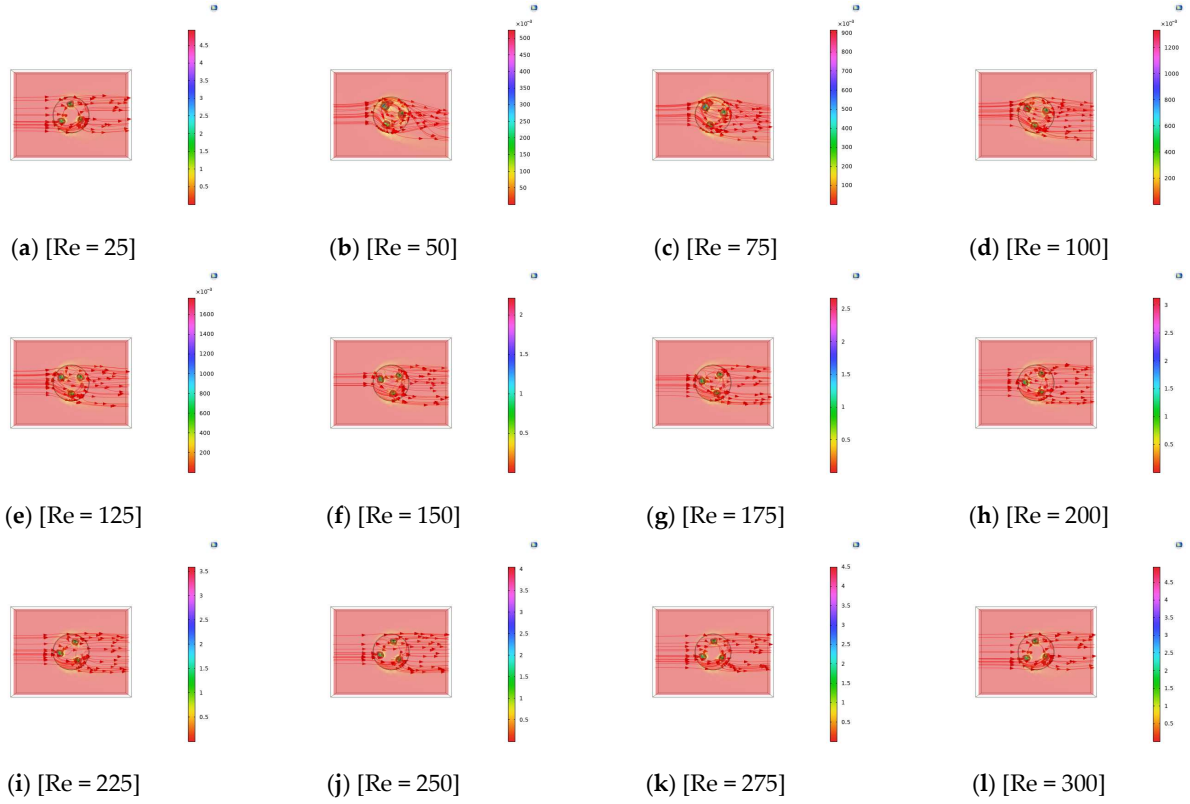


(**a**) [Re = 25] (**b**) [Re = 50] (**c**) [Re = 75] (**d**) [Re = 100]

(**e**) [Re = 125] (**f**) [Re = 150] (**g**) [Re = 175] (**h**) [Re = 200]

(**i**) [Re = 225] (**j**) [Re = 250] (**k**) [Re = 275] (**l**) [Re = 300]

Figure 21. Vorticity contours and streamlines for blade model M6 (RD = +30 mm) at Reynolds number (**a**) 25, (**b**) 50, (**c**) 75, (**d**) 100, (**e**) 125, (**f**) 150, (**g**) 175, (**h**) 200, (**i**) 225, (**j**) 250, (**k**) 275, (**l**) 300.



(**a**) [Re = 25] (**b**) [Re = 50] (**c**) [Re = 75] (**d**) [Re = 100]

(**e**) [Re = 125] (**f**) [Re = 150] (**g**) [Re = 175] (**h**) [Re = 200]

(**i**) [Re = 225] (**j**) [Re = 250] (**k**) [Re = 275] (**l**) [Re = 300]

Figure 22. Vorticity contours and streamlines for blade model M7 (RD = +50 mm) at various Reynolds numbers: (**a**) 25, (**b**) 50, (**c**) 75, (**d**) 100, (**e**) 125, (**f**) 150, (**g**) 175, (**h**) 200, (**i**) 225, (**j**) 250, (**k**) 275, and (**l**) 300.

4. Results and Discussion

This section elaborates on the aerodynamic performance of the seven vertical axis wind turbine blade configurations (M1 to M7) under a range of Reynolds numbers (Re = 25 to 300), reflecting conditions typical of low-speed, small-scale urban wind energy systems. The analysis incorporates critical aerodynamic metrics, including the lift-to-drag ratio (Cl/Cd), pressure coefficient (CoP), power coefficient (Cp), torque coefficient (Ct), and tip speed ratio (TSR). These parameters collectively illuminate how the blade curvature transformation depth (RD) influences turbine efficiency, torque stability, and rotational dynamics.

4.1. Aerodynamic Performance of Blade Configurations

The lift-to-drag ratio (Cl/Cd) fundamentally characterizes the aerodynamic efficiency of the blade configurations by balancing lift generation against parasitic drag forces. This ratio directly influences the mechanical torque and power output of vertical axis wind turbines (VAWTs), particularly in low Reynolds number regimes, where viscous effects and flow separation phenomena are dominant. Our investigation across seven blade profiles, defined by transformation depths (RD) spanning from deeply convex (−50 mm) to highly concave (+50 mm), highlights significant performance variations over Reynolds numbers Re = 25 to 300, which are typical of small-scale urban wind environments. For the deeply convex blade configuration (model M1), the aerodynamic performance initiates with a notably high Cl/Cd value of approximately 1.65 at the lowest Reynolds number of Re = 25. This suggests that the laminar flow was effectively attached with minimal flow separation, resulting in a smooth velocity gradient and a compact wake. At such low Reynolds numbers, viscous forces dominate, and the favorable pressure distribution of the convex curvature prevents early boundary layer detachment, thereby enabling superior

lift production with reduced drag. As the Reynolds number increased, the inertial forces increased, enhancing the turbulence and vortex shedding. Despite this, model M1 sustains relatively high Cl/Cd values, approximately 0.76 at Re = 300, demonstrating its capability to maintain aerodynamic efficiency even as turbulent wake effects intensify. The steady reduction in Cl/Cd with the Reynolds number is consistent with classical fluid mechanics, where an increasing flow velocity escalates boundary layer instabilities; however, the convex profile effectively mitigates these effects by stabilizing flow reattachment and reducing the separation bubble size. Model M2, exhibiting moderate convex curvature (RD = −30 mm), follows a similar aerodynamic trend but with slightly reduced efficiency, starting with Cl/Cd around 1.62 at Re = 25 and maintaining values above 0.80 at Re = 300. The smaller curvature reduced the blade's ability to fully suppress flow separation compared to that of M1, slightly increasing the turbulent wake intensity at higher Reynolds numbers. Nonetheless, M2 preserved a coherent wake and relatively high aerodynamic efficiency, demonstrating the importance of even a modest convex curvature in flow stabilization and drag reduction. Transitioning toward neutral and concave blade shapes, models M3 (RD = −15 mm) and M4 (RD = 0 mm) displayed declining Cl/Cd ratios, beginning near 1.40 and 1.27 at low Reynolds numbers, respectively, and dropping below 0.60 by Re = 100. This rapid decline highlights the early boundary layer separation and increased turbulence stemming from reduced convexity. The concave baseline configuration (M4) particularly suffers from broadened wake zones and unsteady vortex shedding, which increases the aerodynamic drag. These adverse flow features degrade lift production, reduce mechanical torque, and compromise the stability of the power output. Further increasing the concavity of models M5, M6, and M7 markedly deteriorated their aerodynamic efficiency.

Their Cl/Cd ratios begin between 0.95 and 1.08 at Re = 25 but fall sharply, reaching as low as 0.50 for the most concave model, M7, at Re = 300 as shown in Figure 23. These values signify substantial flow separation and turbulent wake development, which increase the aerodynamic losses and produce highly unsteady blade loadings. Concave blade geometries induce strong adverse pressure gradients and thick separation bubbles, which enhance the drag and reduce the effective lift. Consequently, these models suffer from significant reductions in power generation potential and rotational stability under typical operating conditions. The observed variations in Cl/Cd across the blade configurations emphasize the critical role of curvature in controlling the laminar-to-turbulent transition and flow separation dynamics on turbine blades. Convex curvature provides favorable pressure recovery that stabilizes the boundary layer and sustains the attached flow over a broader Reynolds number range, enabling high-lift and low-drag conditions. Conversely, concave curvature fosters early flow detachment and chaotic wake structures, thereby reducing the aerodynamic efficiency and increasing the fatigue-inducing unsteady forces on the rotor. These results align with foundational aerodynamic principles and previous experimental studies, underscoring curvature optimization as a vital design parameter for maximizing the efficiency of low-Re VAWTs.

The pressure coefficient (CoP) reflects the normalized pressure differential across the blade surfaces and is crucial for understanding the aerodynamic loading and flow separation tendencies as shown in Figure 24. For model M1, the CoP reached a maximum of approximately 0.048 at Re = 25, signifying a strong suction effect on the convex blade's suction side and a corresponding pressure differential conducive to lift generation. As the Reynolds number increased, the CoP gradually declined to approximately 0.006 at Re = 300, indicating increased turbulent mixing and a slight reduction in effective aerodynamic loading owing to flow instabilities. Model M2 similarly demonstrated robust pressure gradients with CoP slightly lower than those of M1 but maintained a favorable

aerodynamic loading across the Reynolds number spectrum. The consistent pressure differential supported sustained lift and torque production, despite the onset of moderate turbulence at higher Reynolds numbers. Models M3–M7 exhibited substantially diminished CoP values, particularly at higher Reynolds numbers. The concave blades experienced an early reduction in the pressure differentials, which correlated with the premature boundary layer separation and vortex-induced flow disruptions. In some cases, negative CoP values emerged at elevated Reynolds numbers, indicating reversed or adverse pressure gradients that hindered aerodynamic performance and may have contributed to negative torque or drag-dominated conditions. The decreasing CoP trends with increasing Reynolds number reflect the rising effects of wake turbulence and boundary layer unsteadiness. Convex blade geometries effectively maintain higher pressure differentials, which are critical for lift, whereas concave shapes fail to sustain these differentials, leading to compromised turbine performance. These findings reinforce the importance of the curvature-induced pressure distribution in optimizing the aerodynamic forces on VAWT blades operating in transitional-flow regimes.

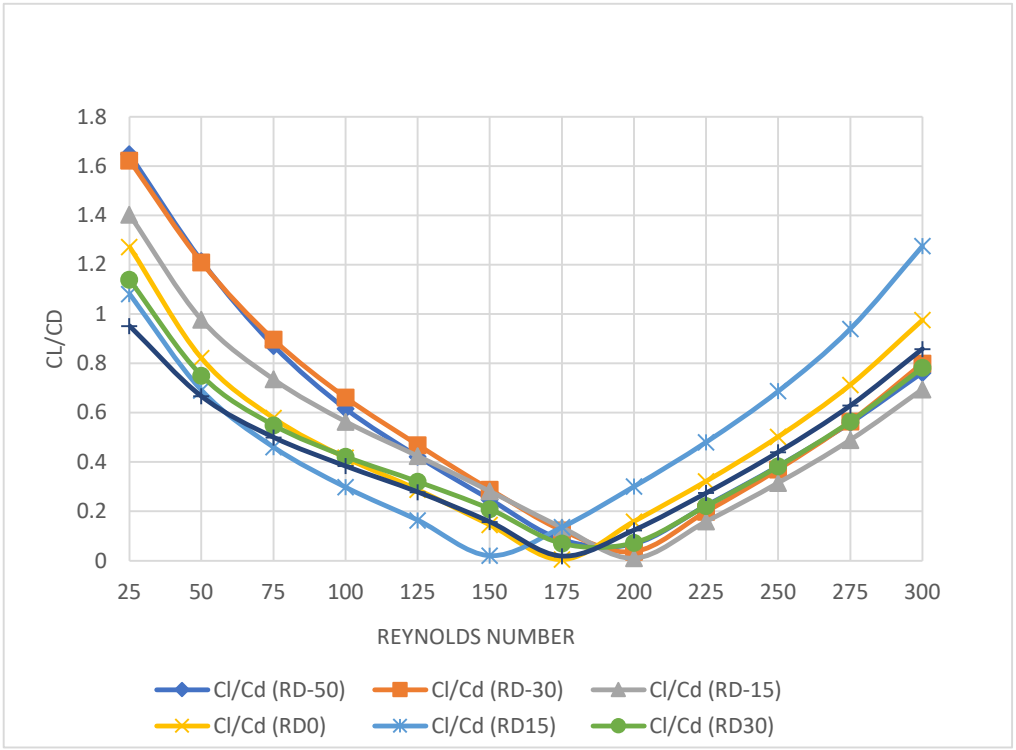


Figure 23. Variation of lift-to-drag ratio (Cl/Cd) with Reynolds number for blade models M1–M7 (RD = −50 mm to +50 mm).

4.2. Power Coefficient and Torque Coefficient Analysis

The power coefficient (Cp) serves as a direct measure of the efficiency with which a vertical axis wind turbine (VAWT) converts the kinetic energy of the incoming wind into mechanical power. Analysis of the power coefficient trends across the seven blade models with varying curvature transformation depths (RD) revealed significant differences that were closely related to blade geometry and flow behavior. Model M1, characterized by the deepest convex curvature (RD = −50 mm), consistently exhibits the highest Cp values over the entire Reynolds number range from 25 to 300. At low Reynolds numbers (Re = 25), Cp started at approximately 0.040, reflecting efficient aerodynamic power extraction facilitated by strong flow attachment and minimal separation on the convex blade surfaces. As the Reynolds number increased, Cp gradually decreased to approx-

imately 0.030 at Re = 300, which aligned with the increased turbulence and flow instabilities expected at higher velocities. However, this gradual decline indicates that the convex blade maintained aerodynamic robustness across both the laminar and transitional flow regimes. The consistently superior Cp performance confirms that the deep convex curvature optimizes the aerodynamic loading, thereby leading to improved power generation potential.

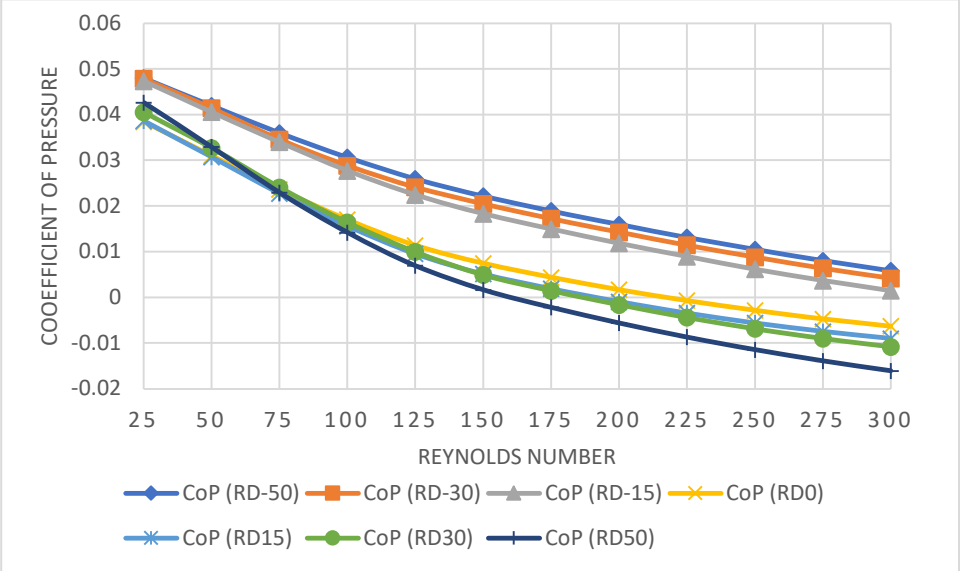


Figure 24. Pressure coefficient (CoP) variation with Reynolds number for blade models M1–M7 (RD = −50 mm to +50 mm).

Model M2 performance were highlighted in Figure 25, with moderate convex curvature (RD = −30 mm), also displays strong Cp values, slightly below model M1 but still significantly outperforming the neutral and concave blades. The Cp for model M2 began close to 0.041 at a low Reynolds number and decreased to approximately 0.025 at the highest Reynolds number tested. This behavior reflects the ability of the moderately convex shape to preserve favorable aerodynamic flow and pressure distributions, reducing drag and sustaining lift. Models M3 and M4, which approach neutral and baseline concave geometries, respectively, demonstrated lower and more rapidly declining Cp values. Model M4, for example, begins with Cp near 0.035 but declines below 0.020 by Re = 300, indicating the loss of aerodynamic efficiency due to earlier flow separation and turbulent wake broadening inherent in concave blade designs. The more concave blades (M5, M6, and M7) performed poorly. Their Cp values started lower (approximately 0.035 to 0.044 at low Reynolds numbers for M5 and M7) and declined sharply as the Reynolds number increased, falling to approximately 0.015 or less at Re = 300. These low values underscore the aerodynamic penalty of concavity: increased drag, unstable wake formation, and diminished lift, all of which impair the turbine's ability to efficiently convert wind energy into mechanical power. The torque coefficient (Ct) provides critical insight into the rotational force generated by the turbine, particularly its starting torque, which determines the rotor's ability to overcome inertia and initiate rotation at low wind speeds. The Ct behavior closely mirrors Cp because torque production is fundamentally linked to aerodynamic forces. Model M1 led to torque generation, with the highest Ct values across the Reynolds number range. At Re = 25, Ct reached approximately 0.067, indicating a strong starting torque that is critical for self-starting performance. This high torque is maintained reasonably well, decreasing to approximately 0.022 at Re = 300, confirming that the convex blade sustains effective rotational forces even as aerodynamic instabilities grow.

This performance suggests that deeply convex blades enhance initial energy conversion, making them ideal for environments with fluctuating or low wind speeds.

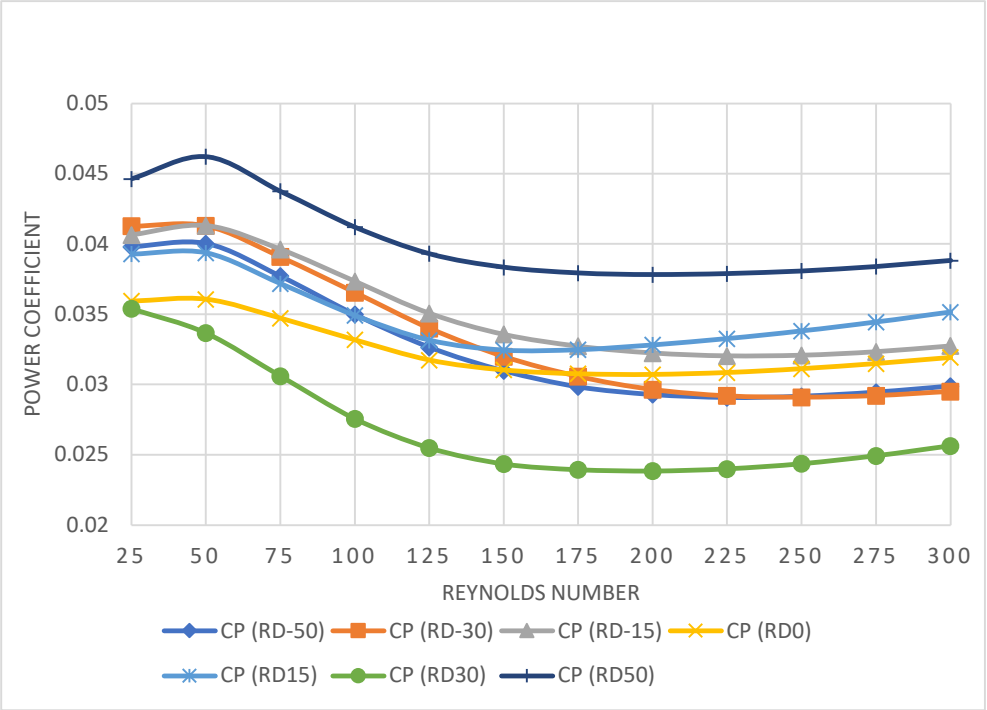


Figure 25. Power coefficient (Cp) variation with Reynolds number for blade models M1 to M7 (transformation depth RD = −50 mm to +50 mm).

Model M2 performance which is shown in Figure 26 also exhibited robust torque generation, with Ct values close to those of M1, although they were slightly reduced. Its Ct at low Reynolds numbers starts near 0.072 and decreases steadily but remains above 0.020 at higher Reynolds numbers, highlighting the efficiency of the moderate convex curvature in sustaining the rotational forces. In contrast, models M3–M7 showed markedly lower and more unstable torque coefficients, reflecting less effective aerodynamic loading and poorer starting torques. The baseline concave blade (M4) experienced a pronounced drop in Ct, indicating difficulties in self-starting and maintaining a stable rotation under low-wind conditions. More concave configurations (M5 through M7) have even lower torque values, with some showing inconsistent behavior, likely caused by turbulent wake interactions and unsteady vortex shedding, which can lead to vibrations and mechanical fatigue. The decline in the torque coefficients of the concave blades aligns with their reduced lift-to-drag ratios and pressure coefficient trends, reinforcing the detrimental impact of the concave geometry on aerodynamic performance and mechanical reliability. Deeply convex blades (models M1 and M2) maximize both the power extraction efficiency and starting torque, enabling better turbine start-up and sustained operation in low Reynolds number environments that are typical of small-scale wind energy systems. Conversely, concave blade shapes suffer from increased aerodynamic drag, flow separation, and turbulent wakes, which significantly degrade power output and torque stability. These findings underscore the importance of curvature optimization in designing efficient and reliable VAWT blades for urban and low-speed-wind applications.

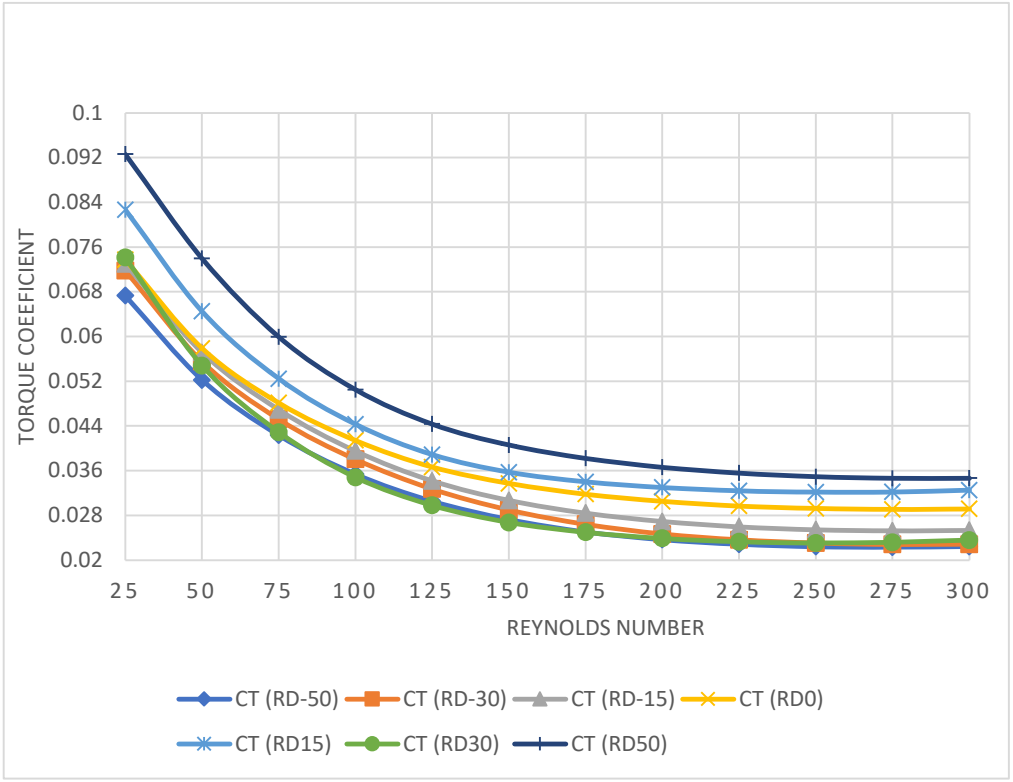


Figure 26. Torque coefficient (Ct) variation with Reynolds number for blade models M1–M7 (transformation depth RD = −50 mm to +50 mm).

4.3. Flow Field and Pressure Distribution

The tip speed ratio (TSR) is a fundamental aerodynamic parameter defined as the ratio of the tangential speed of the blade tip to the free-stream wind velocity. The TSR critically influences the efficiency and mechanical performance of vertical axis wind turbines (VAWTs) because it determines the aerodynamic loading and rotor dynamics under varying wind conditions. Analyzing the TSR across the seven blade models (M1 to M7) which is shown in Figure 27 over Reynolds numbers ranging from 25 to 300 provides vital insights into how blade curvature affects rotor rotational speed and energy capture potential. Convex blade configurations, particularly model M1 (RD = −50 mm), demonstrated the highest TSR values among all the models. At the lowest Reynolds number (Re = 25), M1 achieved a TSR of approximately 0.59, which increased steadily to approximately 1.33 at Re = 300. This increase in the TSR indicates efficient aerodynamic force generation, allowing the rotor to accelerate and maintain higher tip speeds relative to the wind velocity. The convex curvature facilitates a stable lift and minimizes drag, enabling smoother rotational motion and better energy extraction efficiency. Model M2 (RD = −30 mm) shows a comparable TSR trend, starting near 0.57 at low Reynolds numbers and reaching approximately 1.29 at Re = 300. The slight reduction relative to M1 reflects the effect of decreased curvature on the aerodynamic torque and flow attachment, although the blade retained a good rotational responsiveness. Blade models approaching neutral curvature and concave profiles (M3 to M7) displayed lower TSR values across all Reynolds numbers, suggesting reduced aerodynamic torque and a less efficient energy conversion. For instance, the baseline concave blade M4 starts with a TSR of approximately 0.49 at Re = 25 and increases only to approximately 1.10 at Re = 300. Strongly concave blades (M5 to M7) exhibited even lower TSR values, with M7 reaching only approximately 0.48–1.12 over the same Reynolds range. Lower TSRs indicate increased aerodynamic resistance, unsteady flow separation, and less effective rotor acceleration. The overall increase in the TSR with the Reynolds number for

all the blade models reflected the enhanced aerodynamic forces, enabling faster rotor speeds as the wind velocity increased. However, the consistently higher TSR of the convex blades confirmed their superiority in efficiently converting the aerodynamic lift into rotational kinetic energy. From a practical perspective, higher TSR values in convex blades translate into improved mechanical power output and enhanced turbine responsiveness, which are crucial for the startup behavior and energy capture in fluctuating-wind environments. Conversely, a lower TSR in concave blades indicates greater mechanical drag and potential difficulties in achieving self-starting, limiting their effectiveness in small-scale urban wind applications. These TSR results reinforce the earlier findings on aerodynamic efficiency and torque generation, completing a comprehensive picture of how blade curvature governs the aerodynamic and mechanical performance of VAWTs at low Reynolds numbers. Optimizing the curvature toward convex profiles not only improves the lift and drag characteristics but also enhances the rotor dynamics, resulting in turbines that start more easily, operate more smoothly, and generate more power over a wider range of wind conditions.

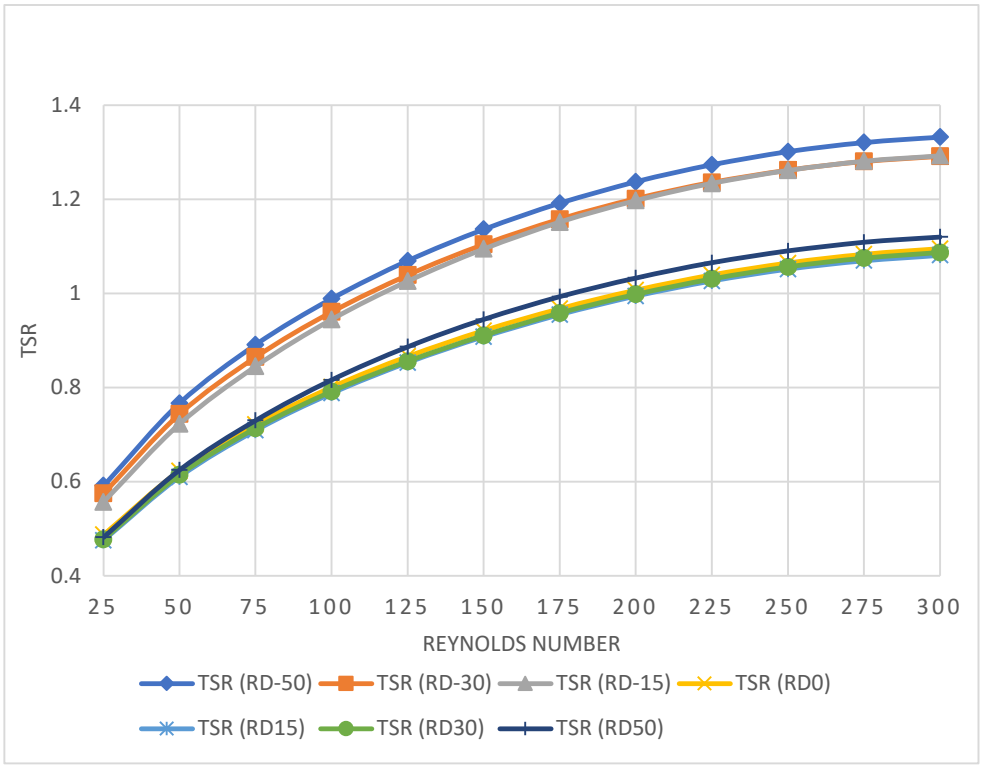


Figure 27. Tip speed ratio (TSR) variation with Reynolds number for blade models M1 to M7 (transformation depth RD = −50 mm to +50 mm).

5. Conclusions

This study presents an extensive numerical investigation of the aerodynamic performance of vertical axis wind turbine (VAWT) blades undergoing systematic curvature transformations, ranging from deeply convex to strongly concave. Employing steady-state computational fluid dynamics (CFD) simulations over a Reynolds number spectrum from 25 to 300, this study elucidates the critical influence of blade curvature on key aerodynamic parameters, including lift-to-drag ratio (Cl/Cd), pressure coefficient (CoP), power coefficient (Cp), torque coefficient (Ct), and tip speed ratio (TSR). Among the seven blade configurations examined, the deeply convex blade model (M1, RD = −50 mm) consistently outperformed the others across the entire Reynolds number range. It exhibits superior lift-to-drag ratios, reflecting stable flow attachment and reduced boundary layer separation, which directly enhance power extraction efficiency and torque generation. The pressure

coefficient analysis corroborated the effectiveness of the convex curvature in maintaining favorable pressure gradients that optimize aerodynamic loading. Moreover, model M1 achieved the highest power and torque coefficients, signifying its capacity to deliver stronger mechanical power and reliable starting torque under low-speed wind conditions, which are typical in urban and small-scale applications. The elevated tip speed ratio across the Reynolds numbers further confirmed the enhanced rotor responsiveness and energy capture capability. Moderately convex blades (model M2, RD = −30 mm) demonstrated slightly reduced yet robust aerodynamic performance, highlighting that even modest convexity significantly benefits flow stability and turbine efficiency. Conversely, the neutral and concave blade configurations (models M3–M7) showed a marked decline in aerodynamic metrics with increasing Reynolds number, which was attributed primarily to early flow separation, turbulent wake broadening, and increased drag. The most concave blade (model M7, RD = +50 mm) consistently yielded the poorest performance, underscoring the aerodynamic disadvantages of excessive concavity in low Reynolds number VAWT operations. These findings establish blade curvature as a pivotal design parameter that governs the aerodynamic efficiency and mechanical reliability of vertical axis VAWTs. Convex blade geometries effectively stabilize laminar boundary layers, minimize flow separation, and promote coherent wake structures, thereby enhancing lift, reducing drag, and improving the torque stability of the rotor blade. Such curvature optimization is essential for advancing the performance and viability of small-scale VAWTs deployed in urban and low-wind environments. In summary, this study provides clear quantitative and qualitative evidence that deep convex blade transformations substantially improve the aerodynamic and mechanical characteristics of Darrieus-type VAWTs at low Reynolds numbers. This insight lays the foundation for future design innovations focused on morphing blades or adaptive curvature mechanisms to optimize performance under varying conditions. The comprehensive parametric data and flow analyses presented in this study will assist researchers and engineers in developing more efficient, reliable, and practical VAWT solutions tailored for decentralized renewable energy generation.

Author Contributions: V.S. significantly contributed to the conception, research design, execution of simulations, data analysis, interpretation, and preparation of the manuscript. V.S.P. supervised the research, provided critical insights, guided analytical approaches, and reviewed and edited the manuscript. M.K.G. and K.R.K. assisted with computational tasks and supported the simulation activities. All authors have read and agreed to the published version of the manuscript.

Funding: This research received no external funding. The APC was funded by the authors.

Data Availability Statement: The data supporting the findings of this study are available from the corresponding author upon reasonable request.

Acknowledgments: The authors acknowledge the technical support provided by the Computational Fluid Dynamics laboratory at Sathyabama Institute of Science and Technology, Chennai, India, and the administrative support from the Department of Mechanical Engineering. During the preparation of this manuscript, the authors used COMSOL Multiphysics version 6.2 for the purposes of numerical simulation and data analysis. The authors have reviewed and edited the output and take full responsibility for the content of this publication.

Conflicts of Interest: The authors declare no conflicts of interest.

Abbreviations

The following abbreviations are used in this manuscript:

VAWT	Vertical Axis Wind Turbine
HAWT	Horizontal Axis Wind Turbine
CFD	Computational Fluid Dynamics
Re	Reynolds Number
Cl/Cd	Lift-to-Drag Ratio
Cp	Power Coefficient
Ct	Torque Coefficient
TSR	Tip Speed Ratio
RD	Transformation Depth
CoP	Pressure Coefficient
URANS	Unsteady Reynolds-Averaged Navier–Stokes
SST	Shear Stress Transport

References

1. Arunvinthan, S.; Nadaraja Pillai, S.; Cao, S. Aerodynamic characteristics of variously modified leading-edge protuberanced (LEP) wind turbine blades under various turbulent intensities. *J. Wind Eng. Ind. Aerodyn.* **2020**, *202*, 104188. [CrossRef]
2. Mohamed, O.S.; Ibrahim, A.A.; Etman, A.K.; Abdelfatah, A.A.; Elbaz, A.M.R. Numerical investigation of Darrieus wind turbine with slotted airfoil blades. *Energy Convers. Manag. X* **2020**, *5*, 100026. [CrossRef]
3. Su, J.; Chen, Y.; Han, Z.; Zhou, D.; Bao, Y.; Zhao, Y. Investigation of V-shaped blade for the performance improvement of vertical axis wind turbines. *Appl. Energy* **2020**, *260*, 114326. [CrossRef]
4. Chrysochoidis-Antsos, N.; Amoros, A.V.; van Bussel, G.J.W.; Mertens, S.M.; van Wijk, A.J.M. Wind resource characteristics and energy yield for micro wind turbines integrated on noise barriers—An experimental study. *J. Wind Eng. Ind. Aerodyn.* **2020**, *203*, 104206. [CrossRef]
5. Siddiqui, M.S.; Khalid, M.H.; Zahoor, R.; Butt, F.S.; Saeed, M.; Badar, A.W. A numerical investigation to analyze effect of turbulence and ground clearance on the performance of a roof top vertical–axis wind turbine. *Renew. Energy* **2021**, *164*, 978–989. [CrossRef]
6. Zhang, Y.; Zhang, X.; Li, Y.; Chang, M.; Xu, J. Aerodynamic performance of a low-Reynolds UAV with leading-edge protuberances inspired by humpback whale flippers. *Chin. J. Aeronaut.* **2021**, *34*, 415–424. [CrossRef]
7. Yan, Y.; Avital, E.; Williams, J.; Cui, J. Aerodynamic performance improvements of a vertical axis wind turbine by leading-edge protuberance. *J. Wind Eng. Ind. Aerodyn.* **2021**, *211*, 104535. [CrossRef]
8. Chen, W.H.; Ocreto, J.B.; Wang, J.S.; Hoang, A.T.; Liou, J.H.; Hwang, C.J.; Chong, W.T. Two-stage optimization of three and four straight-bladed vertical axis wind turbines (SB-VAWT) based on Taguchi approach. *E Prime Adv. Electr. Eng. Electron. Energy* **2021**, *1*, 100025. [CrossRef]
9. Tirandaz, M.R.; Rezaeiha, A. Effect of airfoil shape on power performance of vertical axis wind turbines in dynamic stall: Symmetric Airfoils. *Renew. Energy* **2021**, *173*, 422–441. [CrossRef]
10. Hansen, J.T.; Mahak, M.; Tzanakis, I. Numerical modelling and optimization of vertical axis wind turbine pairs: A scale up approach. *Renew. Energy* **2021**, *171*, 1371–1381. [CrossRef]
11. Nguyen, M.T.; Balduzzi, F.; Goude, A. Effect of pitch angle on power and hydrodynamics of a vertical axis turbine. *Ocean Eng.* **2021**, *238*, 109335. [CrossRef]
12. Francis, M.F.; Ajayi, O.O.; Ojo, J.O. Development of a novel airfoil for low wind speed vertical axis wind turbine using QBlade simulation tool. *Fuel Commun.* **2021**, *9*, 100028. [CrossRef]
13. Kumar, S.; Narayanan, S. Airfoil thickness effects on flow and acoustic characteristics. *Alexandria Eng. J.* **2022**, *61*, 4679–4699. [CrossRef]
14. Lu, B.; Zanj, A. Development of an integrated system design tool for helical Vertical Axis Wind Turbines (VAWT-X). *Energy Rep.* **2022**, *8*, 8499–8510. [CrossRef]
15. Tian, W.; Bian, J.; Yang, G.; Ni, X.; Mao, Z. Influence of a passive upstream deflector on the performance of the Savonius wind turbine. *Energy Rep.* **2022**, *8*, 7488–7499. [CrossRef]
16. Santamaría, L.; Argüelles Díaz, K.M.; Galdo Vega, M.; González Pérez, J.; Velarde-Suárez, S.; Fernández Oro, J.M. Performance assessment of vertical axis wind turbines (VAWT) through control volume theory. *Sustain. Energy Technol. Assess.* **2022**, *54*, 102811. [CrossRef]
17. Gonçalves, A.N.C.; Pereira, J.M.C.; Sousa, J.M.M. Passive control of dynamic stall in a H-Darrieus Vertical Axis Wind Turbine using blade leading-edge protuberances. *Appl. Energy* **2022**, *324*, 119700. [CrossRef]

18. Santamaría, L.; Fernández Oro, J.M.; Argüelles Díaz, K.M.; Meana-Fernández, A.; Pereiras, B.; Velarde-Suárez, S. Novel methodology for performance characterization of vertical axis wind turbines (VAWT) prototypes through active driving mode. *Energy Convers. Manag.* **2022**, *258*, 115530. [CrossRef]
19. Elsakka, M.M.; Ingham, D.B.; Ma, L.; Pourkashanian, M.; Moustafa, G.H.; Elhenawy, Y. Response Surface Optimisation of Vertical Axis Wind Turbine at low wind speeds. *Energy Rep.* **2022**, *8*, 10868–10880. [CrossRef]
20. Teksin, S.; Azginoglu, N.; Akansu, S.O. Structure estimation of vertical axis wind turbine using artificial neural network. *Alexandria Eng. J.* **2022**, *61*, 305–314. [CrossRef]
21. Botero, N.; Ratkovich, N.; Lain, S.; Lopez Mejia, O.D. Synthetic jets as a flow control device for performance enhancement of vertical axis hydrokinetic turbines: A 3D computational study. *Heliyon* **2022**, *8*, e10017. [CrossRef] [PubMed]
22. Maalouly, M.; Souaiby, M.; ElCheikh, A.; Issa, J.S.; Elkhoury, M. Transient analysis of H-type Vertical Axis Wind Turbines using CFD. *Energy Rep.* **2022**, *8*, 4570–4588. [CrossRef]
23. Jooss, Y.; Rønning, E.B.; Hearst, R.J.; Bracchi, T. Influence of position and wind direction on the performance of a roof mounted vertical axis wind turbine. *J. Wind Eng. Ind. Aerodyn.* **2022**, *230*, 105177. [CrossRef]
24. Venkatesan, S.P.; Venkatesh, S.; Kumar, M.S.; Selvan, S.; Sai, Y. Analysis of the blade profile of the Savonius wind turbine using computational fluid dynamics. *Int. J. Ambient Energy* **2022**, *43*, 142–148. [CrossRef]
25. Eltayesh, A.; Castellani, F.; Natili, F.; Burlando, M.; Khedr, A. Aerodynamic upgrades of a Darrieus vertical axis small wind turbine. *Energy Sustain. Dev.* **2023**, *73*, 126–143. [CrossRef]
26. Hamid, H.; Abd El Maksoud, R.M. A comparative examination of the aerodynamic performance of various seashell-shaped wind turbines. *Heliyon* **2023**, *9*, e17036. [CrossRef] [PubMed]
27. Ghiasi, P.; Najafi, G.; Ghobadian, B.; Jafari, A.; Mamat, R.; Ghazali, M.F. CFD-Study of the H-Rotor Darrius wind turbine performance in Drag-Lift and lift Regime: Impact of Type, thickness and chord length of blades. *Alexandria Eng. J.* **2023**, *67*, 51–64. [CrossRef]
28. Geng, F.; Suiker, A.S.J.; Rezaeiha, A.; Montazeri, H.; Blocken, B. A computational framework for the life-time prediction of vertical-axis wind turbines: CFD simulations and high-cycle fatigue modeling. *Int. J. Solids Struct.* **2023**, *284*, 112504. [CrossRef]
29. Zidane, I.F.; Ali, H.M.; Swadener, G.; Eldrainy, Y.A.; Shehata, A.I. Effect of upstream deflector utilization on H-Darrieus wind turbine performance: An optimization study. *Alexandria Eng. J.* **2023**, *63*, 175–189. [CrossRef]
30. Yosry, A.G.; Álvarez, E.Á.; Valdés, R.E.; Pandal, A.; Marigorta, E.B. Experimental and multiphase modeling of small vertical-axis hydrokinetic turbine with free-surface variations. *Renew. Energy* **2023**, *203*, 788–801. [CrossRef]
31. Benmoussa, A.; Páscoa, J.C. Enhancement of a cycloidal self-pitch vertical axis wind turbine performance through DBD plasma actuators at low tip speed ratio. *Int. J. Thermofluids* **2023**, *17*, 100258. [CrossRef]
32. Anggara, B.; Tjahjana, D.D.D.P.; Budiana, E. Numerical Study of Effect of High Efficiency Vortex Addition on Darrieus H Rotor Wind Turbine Performance. *Procedia Struct. Integr.* **2023**, *47*, 675–684. [CrossRef]
33. Gemayel, D.; Abdelwahab, M.; Ghazal, T.; Aboshosha, H. Modelling of vertical axis wind turbine using large eddy simulations. *Results Eng.* **2023**, *18*, 101226. [CrossRef]
34. Rizk, M.; Nasr, K. Computational fluid dynamics investigations over conventional and modified Savonius wind turbines. *Heliyon* **2023**, *9*, e16876. [CrossRef]
35. Shubham, S.; Naik, K.; Sachar, S.; Ianakiev, A. Performance analysis of low Reynolds number vertical axis wind turbines using low-fidelity and mid-fidelity methods and wind conditions in the city of Nottingham. *Energy* **2023**, *279*, 127904. [CrossRef]
36. Singh, E.; Roy, S.; Yam, K.S.; Law, M.C. Numerical analysis of H-Darrieus vertical axis wind turbines with varying aspect ratios for exhaust energy extractions. *Energy* **2023**, *277*, 127739. [CrossRef]
37. Abdolahifar, A.; Azizi, M.; Zanj, A. Flow structure and performance analysis of Darrieus vertical axis turbines with swept blades: A critical case study on V-shaped blades. *Ocean Eng.* **2023**, *280*, 114857. [CrossRef]
38. Ogrodnik, N.; Sudasinghe, A.; Heiber, E.; abo el Ella, H.; Fereidooni, A.; Matida, E.; Kaya, T. Pseudo three-dimensional numerical investigation of legacy vertical axis wind turbine configurations. *Energy Convers. Manag. X* **2023**, *17*, 100338. [CrossRef]
39. Marzec, L.; Buliński, Z.; Krysiński, T.; Tumidajski, J. Structural optimisation of H-Rotor wind turbine blade based on one-way Fluid Structure Interaction approach. *Renew. Energy* **2023**, *216*, 118957. [CrossRef]
40. Li, Y.; Yang, S.; Feng, F.; Tagawa, K. A review on numerical simulation based on CFD technology of aerodynamic characteristics of straight-bladed vertical axis wind turbines. *Energy Rep.* **2023**, *9*, 4360–4379. [CrossRef]
41. Al Noman, A.; Tasneem, Z.; Abhi, S.H.; Badal, F.R.; Rafsanzane, M.; Islam, M.R.; Alam, F. Savonius wind turbine blade design and performance evaluation using ANN-based virtual clone: A new approach. *Heliyon* **2023**, *9*, e15672. [CrossRef]
42. Seifi Davari, H.; Botez, R.M.; Seify Davari, M.; Chowdhury, H.; Hosseinzadeh, H. Blade height impact on self-starting torque for Darrieus vertical axis wind turbines. *Energy Convers. Manag. X* **2024**, *24*, 100814. [CrossRef]
43. Eltayeb, W.A.; Somlal, J. Performance enhancement of Darrieus wind turbines using Plain Flap and Gurney Flap configurations: A CFD analysis. *Results Eng.* **2024**, *24*, 103400. [CrossRef]

44. Eboibi, O.; Eboibi, B.E.O.; Danao, L.A.M. Solidity effects and azimuth angles on flow field aerodynamics and performance of vertical axis wind turbines at low Reynolds number. *Sci. Afr.* **2024**, *24*, e02215. [CrossRef]
45. Campos Rubio, C.V.; Kchaou, M.; de Faria, P.E.; Campos Rubio, J.C.; Alqurashi, F. Development of wind turbines for urban environment using innovative design thinking methodology. *J. Eng. Res.* **2024**. [CrossRef]
46. Silva, P.A.S.F.; Tsoutsanis, P.; Vaz, J.R.P.; Macias, M.M. A comprehensive CFD investigation of tip vortex trajectory in shrouded wind turbines using compressible RANS solver. *Energy* **2024**, *294*, 130929. [CrossRef]
47. Iddou, H.; Bouda, N.N.; Zereg, K. Computational fluid dynamics study on the efficiency of straight-bladed vertical axis wind turbine. *Int. J. Thermofluids* **2024**, *22*, 100672. [CrossRef]
48. Seifi Davari, H.; Botez, R.M.; Seify Davari, M.; Chowdhury, H.; Hosseinzadeh, H. Numerical and experimental investigation of Darrieus vertical axis wind turbines to enhance self-starting at low wind speeds. *Results Eng.* **2024**, *24*, 103240. [CrossRef]
49. Jebelli, A.; Lotfi, N.; Zare, M.S.; Yagoub, M.C.E. A comprehensive review of effective parameters to improve the performance of the Savonius turbine using a computational model and comparison with practical results. *Water Energy Nexus* **2024**, *7*, 266–274. [CrossRef]
50. Javaid, M.T.; ul Hassan, S.S. Power performance optimization of twin vertical axis wind turbine for farm applications. *Wind Energy Eng. Res.* **2024**, *2*, 100005. [CrossRef]
51. Sanaye, S.; Farvizi, A. Optimizing a vertical axis wind turbine with helical blades: Application of 3D CFD and Taguchi method. *Energy Rep.* **2024**, *12*, 2527–2547. [CrossRef]
52. Fatahian, E.; Mishra, R.; Jackson, F.F.; Fatahian, H. Optimization and analysis of self-starting capabilities of vertical axis wind turbine pairs: A CFD-Taguchi approach. *Ocean Eng.* **2024**, *302*, 117614. [CrossRef]
53. Teklemariyem, D.A.; Yimer, E.T.; Ancha, V.R.; Zeru, B.A. Parametric study of an empty diffuser geometric parameters and shape for a wind turbine using CFD analysis. *Heliyon* **2024**, *10*, e26782. [CrossRef]
54. Redchyts, D.; Fernandez-Gamiz, U.; Tarasov, S.; Portal-Porras, K.; Tarasov, A.; Moiseienko, S. Comparison of aerodynamics of vertical-axis wind turbine with single and combine Darrieus and Savonius rotors. *Results Eng.* **2024**, *24*, 103202. [CrossRef]
55. Chen, W.H.; Wang, Y.S.; Chang, M.H.; Show, P.L.; Hoang, A.T. Operation parameter interaction and optimization of vertical axis wind turbine analyzed by Taguchi method with modified additive model and ANOVA. *Energy Rep.* **2024**, *11*, 5189–5200. [CrossRef]
56. Vahidi, D.; Porté-Agel, F. Potential of Wake Scaling Techniques for Vertical-Axis Wind Turbine Wake Prediction. *Energies* **2024**, *17*, 4527. [CrossRef]
57. Abdolahifar, A.; Zanj, A. Addressing VAWT Aerodynamic Challenges as the Key to Unlocking Their Potential in the Wind Energy Sector. *Energies* **2024**, *17*, 5052. [CrossRef]
58. Asim, T.; Osame, P. Startup Dynamics of Drag-Based Multibladed Vertical Axis Wind Turbine. *Eng. Proc.* **2024**, *71*, 1005. [CrossRef]
59. Michna, J.; Rogowski, K. A Refined Approach for Angle of Attack Estimation and Dynamic Force Hysteresis in H-Type Darrieus Wind Turbines. *Energies* **2024**, *17*, 6264. [CrossRef]
60. El Maani, R.; Radi, B.; El Hami, A. Numerical Study and Optimization-Based Sensitivity Analysis of a Vertical-Axis Wind Turbine. *Energies* **2024**, *17*, 6300. [CrossRef]
61. Ghafoorian, F.; Enayati, E.; Mirmotahari, S.R.; Wan, H. Self-Starting Improvement and Performance Enhancement in Darrieus VAWTs Using Auxiliary Blades and Deflectors. *Machines* **2024**, *12*, 0806. [CrossRef]
62. Bang, C.S.; Rana, Z.A.; Prince, S.A. CFD Analysis on Novel Vertical Axis Wind Turbine (VAWT). *Machines* **2024**, *12*, 800. [CrossRef]
63. Mălăel, I.; Strătilă, S. High-Precision Numerical Investigation of a VAWT Starting Process. *Processes* **2024**, *12*, 2263. [CrossRef]
64. Aboujaoude, H.; Polidori, G.; Beaumont, F.; Murer, S.; Toumi, Y.; Bogard, F. Comparative Study of Deflector Configurations under Variable Vertical Angle of Incidence and Wind Speed through Transient 3D CFD Modeling of Savonius Turbine. *Computation* **2024**, *12*, 204. [CrossRef]
65. Altan, G.; Altan, B.D. Effect of Blade Gap Ratio on Turbine Performance in Drag-Based Vertical-Axis Wind Turbines. *Processes* **2024**, *12*, 2215. [CrossRef]
66. Cacciali, L.; Hansen, M.O.L.; Rogowski, K. Highly Stable Lattice Boltzmann Method with a 2-D Actuator Line Model for Vertical Axis Wind Turbines. *Energies* **2024**, *17*, 4847. [CrossRef]
67. Yue, N.; Yang, C.; Li, S. The Influence of Reduced Frequency on H-VAWT Aerodynamic Performance and Flow Field Near Blades. *Energies* **2024**, *17*, 4760. [CrossRef]
68. Zhang, W.; Cao, Y.; Qian, Z.; Wang, J.; Zhu, Y.; Yang, Y.; Wang, Y.; Wu, G. Research on Aerodynamic Performance of Asynchronous-Hybrid Dual-Rotor Vertical-Axis Wind Turbines. *Energies* **2024**, *17*, 4424. [CrossRef]
69. Yang, Y.; Cao, Y.; Qian, Z.; Wang, J.; Zhu, Y.; Chen, X.; Zhang, W.; Wang, Y.; Wu, G.; Chen, S. A Study on the Effect of Turbulence Intensity on Dual Vertical-Axis Wind Turbine Aerodynamic Performance. *Energies* **2024**, *17*, 4124. [CrossRef]
70. Hammad, M.A.; Mahmoud, A.M.; Abdelrhman, A.M.; Sarip, S. Performance Enhancement of H-Type Darrieus VAWT Using a Hybrid Method of Blade Pitch Angle Regulation. *Energies* **2024**, *17*, 4044. [CrossRef]

71. Chitura, A.G.; Mukumba, P.; Lethole, N. Enhancing the Performance of Savonius Wind Turbines: A Review of Advances Using Multiple Parameters. *Energies* **2024**, *17*, 3708. [CrossRef]
72. Escudero Romero, A.; Blasetti, A.P.; Acosta-López, J.G.; Gómez-García, M.Á.; de Lasa, H. Vorticity and Its Relationship to Vortex Separation, Dynamic Stall, and Performance, in an H-Darrieus Vertical-Axis Wind Turbine Using CFD Simulations. *Processes* **2024**, *12*, 1556. [CrossRef]
73. Gurusamy, M.K.; P M, D.M.; R R, R.; S, V. Numerical simulation and optimization of sweep angle and depth variation studies for enhanced performance of Savonius turbine. *J. Mech. Eng. Autom. Control Syst.* **2025**. [CrossRef]
74. Oliveira, T.D.; Tofaneli, L.A.; Santos, A.Á.B. Aerodynamic optimization of small diffuser Augmented Wind Turbines: A differential evolution approach. *Energy Convers. Manag. X* **2025**, *26*, 100891. [CrossRef]
75. Arrieta-Gomez, M.; Vélez-García, S.; Hincapié Zuluaga, D.; Tejada, J.C.; Sanin-Villa, D. Efficiency optimization of a hybrid Savonius-Darrieus hydrokinetic turbine via regression modeling and CFD-based design of experiments. *Results Eng.* **2025**, *27*, 105751. [CrossRef]
76. Gupta, A.; Ali, U.; Abderrahmane, H.A.; Janajreh, I. Blade pitching in vertical axis wind turbines: A double multiple stream tube theoretical approach to performance enhancement. *Heliyon* **2025**, *11*, e42101. [CrossRef] [PubMed]
77. Ghafoorian, F.; Mirmotahari, S.R.; Eydizadeh, M.; Mehrpooya, M. A systematic investigation on the hybrid Darrieus-Savonius vertical axis wind turbine aerodynamic performance and self-starting capability improvement by installing a curtain. *Next Energy* **2025**, *6*, 100203. [CrossRef]
78. Liu, Q.; Bashir, M.; Huang, H.; Miao, W.; Xu, Z.; Yue, M.; Li, C. Nature-inspired innovative platform designs for optimized performance of Floating vertical Axis wind turbines. *Appl. Energy* **2025**, *380*, 125120. [CrossRef]
79. Mohamed, O.S.; Melani, P.F.; Soraperra, G.; Brighenti, A.; Ferrara, G.; Betti, V.; Balduzzi, F.; Bianchini, A. Development of a computationally efficient CFD model for vertical-axis hydrokinetic turbines: A critical assessment. *Ocean Eng.* **2025**, *324*, 120692. [CrossRef]
80. Rusli, C.C.; Kong, K.K.; Khoo, S.Y.; Long, S.X.; Chong, W.T. Performance enhancement of cross-axis-wind-turbine: Design and CFD analysis of an omni-directional flow concentrator. *Alexandria Eng. J.* **2025**, *127*, 500–521. [CrossRef]
81. Nugraha, A.D.; Garingging, R.A.; Wiranata, A.; Sitanggang, A.C.; Supriyanto, E.; Tanbar, F.; Muflikhun, M.A. Comparison of 'Rose, Aeroleaf, and Tulip' vertical axis wind turbines (VAWTs) and their characteristics for alternative electricity generation in urban and rural areas. *Results Eng.* **2025**, *25*, 103885. [CrossRef]
82. Rogowski, K.; Michna, J.; Mikkelsen, R.F.; Ferreira, C.S. Impact of zigzag tape on blade loads and aerodynamic wake in a vertical axis wind turbine: A Delft VAWT case study. *Energy* **2025**, *321*, 135344. [CrossRef]
83. Abdolahifar, A.; Montazeri, H.; Zanj, A. Towards enhanced startup performance of Darrieus vertical-axis wind turbines: Key flow features at moderate tip speed ratios. *Renew. Energy* **2025**, *256*, 123778. [CrossRef]
84. Sridhar, S. Performance enhancement of Ducted Wind Turbines under yawed flow using optimized tubercled ducts: An investigative study. *Energy Convers. Manag.* **2025**, *333*, 119764. [CrossRef]
85. Shen, W.; Xie, T.; Ge, L.; Yin, J.; Sun, Z. Determination of angle of attack and dynamic stall loop in the complex vortical flow of a vertical axis wind turbine. *Theor. Appl. Mech. Lett.* **2025**, *15*, 100560. [CrossRef]
86. Priyadumkol, J.; Muangput, B.; Namchanthra, S.; Zin, T.; Phengpom, T.; Chookaew, W.; Suvanjumrat, C.; Promtong, M. CFD modelling of vertical-axis wind turbines using transient dynamic mesh towards lateral vortices capturing and Strouhal number. *Energy Convers. Manag. X* **2025**, *26*, 101022. [CrossRef]
87. Kalassov, N.; Baizhuma, Z.; Manatbayev, R.; Yershina, A.; Isataev, M.; Kalassova, A.; Seidulla, Z.; Bektibay, B.; Amir, B. Integrated Approach to Aerodynamic Optimization of Darrieus Wind Turbine Based on the Taguchi Method and Computational Fluid Dynamics (CFD). *Appl. Sci.* **2025**, *15*, 5739. [CrossRef]
88. Leithead, W.E.; Amiri, A.M.K.; Camciuc, A.; Morgan, L.; Carroll, J.; Feuchtwang, J. X-Rotor, an Innovative Offshore Wind Turbine to Reduce Cost of Energy. *Energies* **2025**, *18*, 2549. [CrossRef]
89. Zhang, T.; Wang, G.; Li, Q. Effects of a J-Shaped Blade on the Performance of a Vertical-Axis Wind Turbine Using the Improved Delayed Detached Eddy Simulation Method. *Machines* **2025**, *13*, 403. [CrossRef]
90. Ghafoorian, F.; Hosseini Rad, S.; Moghimi, M. Enhancing Self-Starting Capability and Efficiency of Hybrid Darrieus–Savonius Vertical Axis Wind Turbines with a Dual-Shaft Configuration. *Machines* **2025**, *13*, 87. [CrossRef]
91. Asim, T.; Amber, I.; Singh, D.; Siddiqui, M.S. Numerical Investigations on the Effects of Inertia on the Startup Dynamics of a Multibladed Savonius Wind Turbine. *Energies* **2025**, *18*, 1638. [CrossRef]
92. Ridho, M.H.; Prabowo. Validate CFD Simulation of H-Darrieus Vertical Axis Wind Turbine (VAWT) with Experimental Data. *Eng. Proc.* **2025**, *84*, 53. [CrossRef]
93. Elbeji, T.; Ben Amira, W.; Souaissa, K.; Ghiss, M.; Bentaher, H.; Ben Fredj, N. Three-Dimensional Aeroelastic Investigation of a Novel Convex Bladed H-Darrieus Wind Turbine Based on a Two-Way Coupled Computational Fluid Dynamics and Finite Element Analysis Approach. *Fluids* **2025**, *10*, 17. [CrossRef]

94. Nunez, E.E.; García González, D.; López, O.D.; Casas Rodríguez, J.P.; Laín, S. Fluid–Structure Interaction of a Darrieus-Type Hydrokinetic Turbine Modified with Winglets. *J. Mar. Sci. Eng.* **2025**, *13*, 548. [CrossRef]
95. Hara, Y.; Moral, M.S.; Ide, A.; Jodai, Y. Fast Simulation of the Flow Field in a VAWT Wind Farm Using the Numerical Data Obtained by CFD Analysis for a Single Rotor. *Energies* **2025**, *18*, 220. [CrossRef]
96. Moreno, M.; Trejo-Zúñiga, I.; Terrazas, J.; Díaz-Ponce, A.; Pérez-Terrazo, A. Hybridization of a Micro-Scale Savonius Rotor Using a Helical Darrieus Rotor. *Fluids* **2025**, *10*, 63. [CrossRef]
97. Lisowski, F.; Augustyn, M. Analytical and Computational Fluid Dynamics Methods for Determining the Torque and Power of a Vertical-Axis Wind Turbine with a Carousel Rotor. *Appl. Sci.* **2025**, *15*, 208. [CrossRef]
98. Wang, Q.; Zhang, Z. Airfoil Optimization Design of Vertical-Axis Wind Turbine Based on Kriging Surrogate Model and MIGA. *Energies* **2025**, *18*, 927. [CrossRef]
99. Ghafoorian, F.; Wan, H. Impact of Passive Modifications on the Efficiency of Darrieus Vertical Axis Wind Turbines Utilizing the Kline-Fogleman Blade Design at the Trailing Edge. *Energies* **2025**, *18*, 718. [CrossRef]
100. Fazylova, A.; Alipbayev, K.; Iliev, T.; Kaliyeva, N. Adaptive Control of the Aerodynamic Flaps of the Savonius Rotor Under Variable Wind Loads. *Appl. Sci.* **2025**, *15*, 6096. [CrossRef]
101. Chen, S.; Song, C.; Qian, Z.; Wu, A.; Zhu, Y.; Xia, J.; Wang, J.; Yang, Y.; Chen, X.; Yuan, Y.; et al. Improvement of Modified Rotor on Aerodynamic Performance of Hybrid Vertical Axis Wind Turbine. *Energies* **2025**, *18*, 3357. [CrossRef]
102. Ali, S.; Park, H.; Lee, D. Structural Optimization of Vertical Axis Wind Turbine (VAWT): A Multi-Variable Study for Enhanced Deflection and Fatigue Performance. *J. Mar. Sci. Eng.* **2025**, *13*, 19. [CrossRef]

Disclaimer/Publisher's Note: The statements, opinions and data contained in all publications are solely those of the individual author(s) and contributor(s) and not of MDPI and/or the editor(s). MDPI and/or the editor(s) disclaim responsibility for any injury to people or property resulting from any ideas, methods, instructions or products referred to in the content.